Kent Academic Repository

Astronomy & Astrophysics

A global view on star formation: The GLOSTAR Galactic plane survey

X. Galactic H II region catalog using radio recombination lines[*]

S. Khan[1],[**][ID], M. R. Rugel[1,2,3],[***][ID], A. Brunthaler[1][ID], K. M. Menten[1], F. Wyrowski[1], J. S. Urquhart[4][ID], Y. Gong[1][ID], A. Y. Yang[5,6,1][ID], H. Nguyen[1][ID], R. Dokara[1][ID], S. A. Dzib[1][ID], S.-N. X. Medina[1,7][ID], G. N. Ortiz-León[8,1][ID], J. D. Pandian[9][ID], H. Beuther[10][ID], V. S. Veena[1,11][ID], S. Neupane[1][ID], A. Cheema[1][ID], W. Reich[1][ID], and N. Roy[12]

[1] Max-Planck-Institut für Radioastronomie, Auf dem Hügel 69, 53121 Bonn, Germany
  e-mail: skhan@mpifr-bonn.mpg.de
[2] Center for Astrophysics | Harvard & Smithsonian, 60 Garden Street, Cambridge, MA 02138, USA
[3] National Radio Astronomy Observatory, PO Box O, 1003 Lopezville Road, Socorro, NM 87801, USA
[4] Centre for Astrophysics and Planetary Science, University of Kent, Canterbury CT2 7NH, UK
[5] National Astronomical Observatories, Chinese Academy of Sciences, A20 Datun Road, Chaoyang District, Beijing 100101, PR China
[6] Key Laboratory of Radio Astronomy and Technology, Chinese Academy of Sciences, A20 Datun Road, Chaoyang District, Beijing 100101, PR China
[7] German Aerospace Center, Scientific Information, 51147 Cologne, Germany
[8] Instituto Nacional de Astrofísica, Óptica y Electrónica, Apartado Postal 51 y 216, 72000 Puebla, Mexico
[9] Department of Earth & Space Sciences, Indian Institute of Space Science and Technology, Trivandrum 695547, India
[10] Max Planck Institute for Astronomy, Koenigstuhl 17, 69117 Heidelberg, Germany
[11] I. Physikalisches Institut, Universität zu Köln, Zülpicher Str. 77, 50937 Köln, Germany
[12] Department of Physics, Indian Institute of Science, Bangalore 560012, India

ABSTRACT

Studies of Galactic H II regions are of crucial importance for studying star formation and the evolution of the interstellar medium. Gaining an insight into their physical characteristics contributes to a more comprehensive understanding of these phenomena. The GLOSTAR project aims to provide a GLObal view on STAR formation in the Milky Way by performing an unbiased and sensitive survey. This is achieved by using the extremely wideband (4–8 GHz) *C*-band receiver of the *Karl G. Jansky* Very Large Array and the Effelsberg 100 m telescope. Using radio recombination lines observed in the GLOSTAR survey with the VLA in D-configuration with a typical line sensitivity of $1\sigma \sim 3.0$ mJy beam^{-1} at ~5 km s^{-1} and an angular resolution of $25''$, we cataloged 244 individual Galactic H II regions ($-2° \le \ell \le 60°$ and $|b| \le 1°$, and $76° \le \ell \le 83°$ and $-1° \le b \le 2°$) and derived their physical properties. We examined the mid-infrared (MIR) morphology of these H II regions and find that a significant portion of them exhibit a bubble-like morphology in the GLIMPSE 8 μm emission. We also searched for associations with the dust continuum and sources of methanol maser emission, other tracers of young stellar objects, and find that 48% and 14% of our H II regions, respectively, are coextensive with those. We measured the electron temperature for a large sample of H II regions within Galactocentric distances spanning from 1.6 to 13.1 kpc and derived the Galactic electron temperature gradient as $\sim 372 \pm 28$ K kpc^{-1} with an intercept of 4248 ± 161 K, which is consistent with previous studies.

Key words. instrumentation: interferometers – catalogs – surveys – stars: formation – H II regions

1. Introduction

H II regions are the zones of ionized plasma formed when the ultraviolet (UV) radiation emitted by massive stars of spectral type B0 or earlier ionizes the surrounding interstellar medium (ISM). Since these massive stars have lifespans as short as a

few million years, the presence of H II regions serves as a strong indication of recent high-mass star formation (HMSF) activity within the Galaxy. Despite their small numbers and short existence, these regions play a crucial role in the dynamics and evolution of the ISM and the Galaxy as a whole. H II regions act as classic indicators of Galactic spiral arms and have played a fundamental role in enhancing our knowledge of our Galaxy's structure (e.g., Georgelin & Georgelin 1976; Reid et al. 2019). The chemical abundances within these regions represent the current abundances of the Galaxy, illustrating Galactic chemical evolution. The central stars not only emit a substantial amount of UV and far-ultraviolet (FUV) photons into their surroundings, but also provide feedback mechanisms that influence the subsequent generation of star formation in a sequential manner

---

(Elmegreen & Lada 1977; Deharveng et al. 2003; Brand et al. 2011; Thompson et al. 2012).

Young and dense H II regions, including hypercompact (HC) and ultracompact (UC) H II regions, are powered by massive young stars that are embedded within dusty molecular cocoons. These cocoons are optically thick to visible and UV radiation emitted by the massive young star. As H II regions evolve, they progressively disperse the surrounding material. H II regions harbor a substantial amount of dust that can absorb a significant portion of the UV radiation emitted by their central OB stars (Yang et al. 2021; Binder & Povich 2018; Wood & Churchwell 1989). These absorbed photons are re-emitted at infrared wavelengths. As a result, H II regions exhibit a characteristic mid-infrared (MIR) signature, with emission from polycyclic aromatic hydrocarbons (PAHs), in the ~4 to 12 μm wavelength range, typically enclosing the 24 μm continuum emission from warm dust, which coexists with the ionized gas traced by radio continuum emission (see Anderson et al. 2011). The distinctive MIR emission has been utilized to identify potential H II region candidates (e.g., Anderson et al. 2014), which can subsequently be validated through observations of radio continuum and radio recombination lines (RRLs).

The radio continuum emission from H II regions is thermal bremsstrahlung, which makes them bright at radio wavelengths. Emission from recombining electrons and nuclei in the plasma produces recombination lines, observable from optical to radio wavelengths. Emission from RRLs is a valuable tool to confirm the presence of H II regions. They facilitate the exploration of the physical conditions and, given their Doppler velocities, the dynamics of ionized gas within these regions (Brown et al. 1978; Gordon & Sorochenko 2002). Additionally, measuring the velocities of RRLs as probes of Galactic rotation enables the determination of "kinematic distances" to H II regions. The relationship between the electron temperatures derived from RRL measurements and Galactocentric distances reveals a Galactic temperature and metallicity gradient (Churchwell & Walmsley 1975; Shaver et al. 1983; Wink et al. 1983; Quireza et al. 2006). The metallicity gradient imposes significant constraints on the chemical evolution of the Galaxy (Balser et al. 2015; Wenger et al. 2019). Finally, with a large sample, we can statistically investigate the physical characteristics of Galactic H II regions.

In the past, extensive radio continuum and RRLs surveys have unveiled a large number of Galactic H II regions (e.g., Reifenstein et al. 1970; Altenhoff et al. 1979; Lockman 1989; Kuchar & Clark 1997; Urquhart et al. 2007, 2009, 2013; Kalcheva et al. 2018; Gao et al. 2019; Chen et al. 2020b). Paladini et al. (2003) created a widely used master catalog of 1442 sources by compiling radio data of Galactic H II regions from 24 published works. The Green Bank Telescope H II Region Discovery Survey (GBT HRDS; Bania et al. 2010; Anderson et al. 2011) doubled the number of known H II regions in the Galactic zone $343° \leq \ell \leq 67°$, $|b| \leq 1°$, by detecting RRLs from 448 previously unknown H II regions. Similarly, Bania et al. (2012) conducted an RRL survey with the Arecibo telescope and identified 37 new H II regions. Despite these efforts, the census of Galactic H II regions remains incomplete, as is indicated by GBT HRDS. In response, Anderson et al. (2014) compiled a catalog of around 8000 Galactic H II region and H II region candidates using data from the all-sky Wide-Field Infrared Survey Explorer (WISE; Wright et al. 2010).

The GLObal view on STAR Formation (GLOSTAR[1]) in the Milky Way survey (Medina et al. 2019; Brunthaler et al. 2021)

is an unbiased survey observing the Galactic plane with the *Karl G. Jansky* Very Large Array (VLA) in D- and B-configurations as well as the Effelsberg 100 m radio telescope at *C*-band (4–8 GHz). The survey comprises observations of the continuum emission in full polarization and of spectral lines (namely, the 4.8 GHz transition of formaldehyde (H_2CO), the 6.7 GHz maser line of methanol (CH_3OH) maser and numerous RRLs) in order to locate and characterize star-forming regions in the Milky Way. The data contains a wealth of information that has already been used to catalog radio sources (Medina et al. 2019, 2024; Dzib et al. 2023; Yang et al. 2023), identify supernova remnants (SNRs; Dokara et al. 2021, 2023), increase the number of class II methanol masers (Ortiz-León et al. 2021; Nguyen et al. 2022), study radio emission of young stellar objects (YSOs) in the Galactic center (Nguyen et al. 2021), and understand the molecular gas structures on different linear scales with the 4.8 GHz formaldehyde (H_2CO) absorption line in the Cygnus X region (Gong et al. 2023). This work uses RRL data observed in the GLOSTAR survey to investigate Galactic H II regions and their physical properties.

In this study, we present a catalog of Galactic H II regions distributed over a significant part of the Galactic plane toward which RRL emission was detected in the GLOSTAR survey. We structure this paper as follows. In Sect. 2, we describe the GLOSTAR observations, the imaging processes, and also the ancillary data used in the paper. Section 3 details our source extraction criteria and methods. Section 4 describes the sources catalog and the physical properties of the H II regions and provides comparisons with previous studies. In Sect. 5, we discuss our findings. We present a summary in Sect. 6.

2. Observations and data analysis

2.1. VLA D-configuration observations

The GLOSTAR survey (Brunthaler et al. 2021) was carried out using the VLA in B- and D-configuration and the Effelsberg 100 m radio telescope in the 4–8 GHz frequency range (*C*-band). The above paper gives a comprehensive, detailed description of the survey and first results, while a summary follows here. The full survey covers the Galactic longitude range of $-2° \leq \ell \leq 60°$ with latitudes $|b| \leq 1°$ and, in addition, the Cygnus X region ($76° \leq \ell \leq 83°$, $-1° \leq b \leq 2°$), or 145 square degrees in total. The data products from the survey include continuum emission from the 4.2–5.2 GHz and 6.4–7.4 GHz ranges in full polarization. Higher-frequency-resolution spectral windows were used to cover the most prominent methanol maser emission line at 6.7 GHz ($5_1 - 6_0A^+$), seven hydrogen RRLs, and the 4.829 GHz ($1_{1,0}-1_{1,1}$) transition of formaldehyde. The lines were observed in the dual polarization mode with channel spacing of 3.9 kHz for CH_3OH and H_2CO, and 62.5 kHz for the RRLs. The details of RRL observations using VLA in D-configuration are summarized in Table 1. The central band velocity with respect to the local standard of rest, V_{LSR}, was varied for different regions of the survey based on longitude-velocity plots of CO in the Milky Way (e.g., Dame et al. 2001). The observations providing the data used in this work were carried out using 380 h of VLA observing time during the time period from December 2011 to April 2017. Further details with program IDs are summarized in Table 1 of Ortiz-León et al. (2021), Nguyen et al. (2022) and Medina et al. (2024). While the GLOSTAR survey provides *C*-band RRL observations using the VLA in both B and D configurations and the Effelsberg 100 m telescope, our focus is mainly on the VLA D configuration RRL data. Initial tests on

---

[1] https://glostar.mpifr-bonn.mpg.de/glostar/

Table 1. Observed RRLs, bandwidth, number of channels, spectral resolution, and velocity coverage of VLA observations.

RRL	Frequency (MHz)	Bandwidth (MHz)	Channels	Resolution (km s^{-1})	Coverage (km s^{-1})
H114α	4380.954	8	128	4.3	547
H113α	4497.776	8	128	4.2	533
H112α	4618.789	8	128	4.1	529
H110α	4874.157	8	128	3.8	492
H99α	6676.076	8	128	2.8	359
H98α	6881.486	8	128	2.7	348
H96α [(*)]	7318.296	8	128	2.5	328

Notes. For $\ell = 58°–60°$, the RRLs H115α (4268.142 MHz), H102α (6106.855 MHz), and H103α (5931.544 MHz) were observed instead of H110α and H96α. [(*)]The H96α transition was flagged for the entire survey area due to RFI contamination.

the VLA B-configuration RRL data revealed detections only for the most prominent star-forming regions in our survey area. For most of the regions in this work, the data is heavily affected by spatial filtering and not sensitive enough to detect RRL emission. While adding Effelsberg 100 m RRL data could help fill in the missing flux, we find many large and diffuse H II regions in the Effelsberg 100 m data, which are significantly fainter and more extended scales than traced by the VLA D-configuration data presented here. Sources detected in the Effelsberg 100 m data will be discussed in a separate publication after completion of processing, and we shall include comparisons to the VLA D-configuration where applicable. In this work, we focus on RRL emission from H II regions on scales of ~0.1–10 pc traced by the VLA D-configuration data.

2.2. Data reduction and imaging

In this work, we focus on RRL data obtained within the GLOSTAR survey conducted with the VLA in D-configuration. The data underwent calibration using a modified version of the VLA scripted pipeline[2] (version 1.3.8) for CASA[3] (version 4.6.0) designed for spectral line data. To preserve spectral resolution, no Hanning smoothing was applied during the preliminary calibration. The `rflag` flagging command was selectively used solely for calibration scans to avoid erroneous flagging of spectral lines. Furthermore, `statwt` was not used to alter the statistical weighting. The complex gain calibrators used for different fields include: J1804+0101, J1820–2528, J1811–2055, J1825–0737, J1907+0127, J1955+1530, J1925+2106, and J1931+2243, and the flux calibrators are 3C286 and 3C48. After the initial execution of the calibration pipeline, quality checks, manual flagging, and a rerun of the pipeline were carried out to ensure data integrity. The RRLs were imaged individually in fields with dimensions of $\Delta\ell \times \Delta b = 1° \times 2°$, except for the Cygnus X region in which the image dimensions were adjusted to $1° \times 3°$. To ensure consistent sensitivity across the image borders and account for sources with potential sidelobe effects, we incorporated neighboring pointings during the imaging process. We subtracted the continuum in the *uv*-domain from line-free channels. As line-free channels, we chose all channels excluding velocities between –40 and 120 km s^{-1} for $\ell \geq 9°$, and –40 and 100 km s^{-1} for $\ell \leq 9°$ as the pure continuum emission. For a few tiles toward the Galactic center,

the channels were selected manually. The line-free continuum and line data were separately imaged and deconvolved with the CASA (version 5.7.0) task `tclean`, with subparameters `robust=0.5`, `imagemode="mosaic"`, `gridder="mosaic"`, and `restoringbeam="common"` to restore the common beam. We flagged the higher-frequency H96α line data for the entire survey area due to high contamination from radio frequency interference (RFI) before imaging (for more details see Brunthaler et al. 2021). Other lines that were affected in subsets of the survey are: H99α for the fields centered at $\ell = 17.5°$ and $\ell=36.5°$; H98α, which were flagged at $\ell = 37.5°$; the H113α transition, which was flagged for $\ell = 54.5°$; and the H112α transition, for $\ell = 56.5°$. The removal was done using a combination of the automatic flagging routines `rflag` and `tfcrop` prior to imaging within the CASA environment.

Previous studies (e.g., Balser 2006; Alves et al. 2010; Anderson et al. 2011; Beuther et al. 2016; Chen et al. 2020b) have shown that multiple higher-principle quantum number RRLs (n > 50) can be averaged together to improve the signal-to-noise ratio. Because RRLs with adjacent quantum numbers and the same quantum number difference, $\triangle$n, arise from similar energy levels and have similar oscillator strengths, their line parameters such as intensity, line width, and velocity are nearly identical. Khan et al. (2022) successfully used the GLOSTAR stacked RRLs to study the physical properties of the ionized gas in the W33 Main star-forming region. Thus, we averaged the data of all six observed RRLs to get a more sensitive composite $\langle$Hn$\alpha\rangle$ RRL. However, before stacking RRLs, we re-gridded all the line image cubes to common velocity bins of 5 km s^{-1} with a velocity range from –150 km s^{-1} to 150 km s^{-1}, and smoothed the data to a common angular resolution of 25″. Fig. 1 provides radio continuum images, corresponding MIR color composite images, and $\langle$Hn$\alpha\rangle$ spectra for three distinct H II regions. G049.205−0.342 and G032.797+0.191 exemplify extended and compact H II regions found in our catalog, respectively, while G028.687+0.177 represents the weakest source within our catalog.

In the GLOSTAR VLA survey, *C*-band continuum emission was observed with two 1 GHz basebands in full polarization mode and imaged at an average frequency of 5.8 GHz (see Medina et al. 2019; Brunthaler et al. 2021). Images produced from line-free portions of the bands were used to determine the continuum flux density of the sources, which was used to derive physical properties such as the electron temperature, electron density, emission measure (EM), and Lyman continuum photon rate (see Sect. 4.3). While the sensitivity of the full 2 GHz continuum surpasses that of the line-free continuum, we benefit
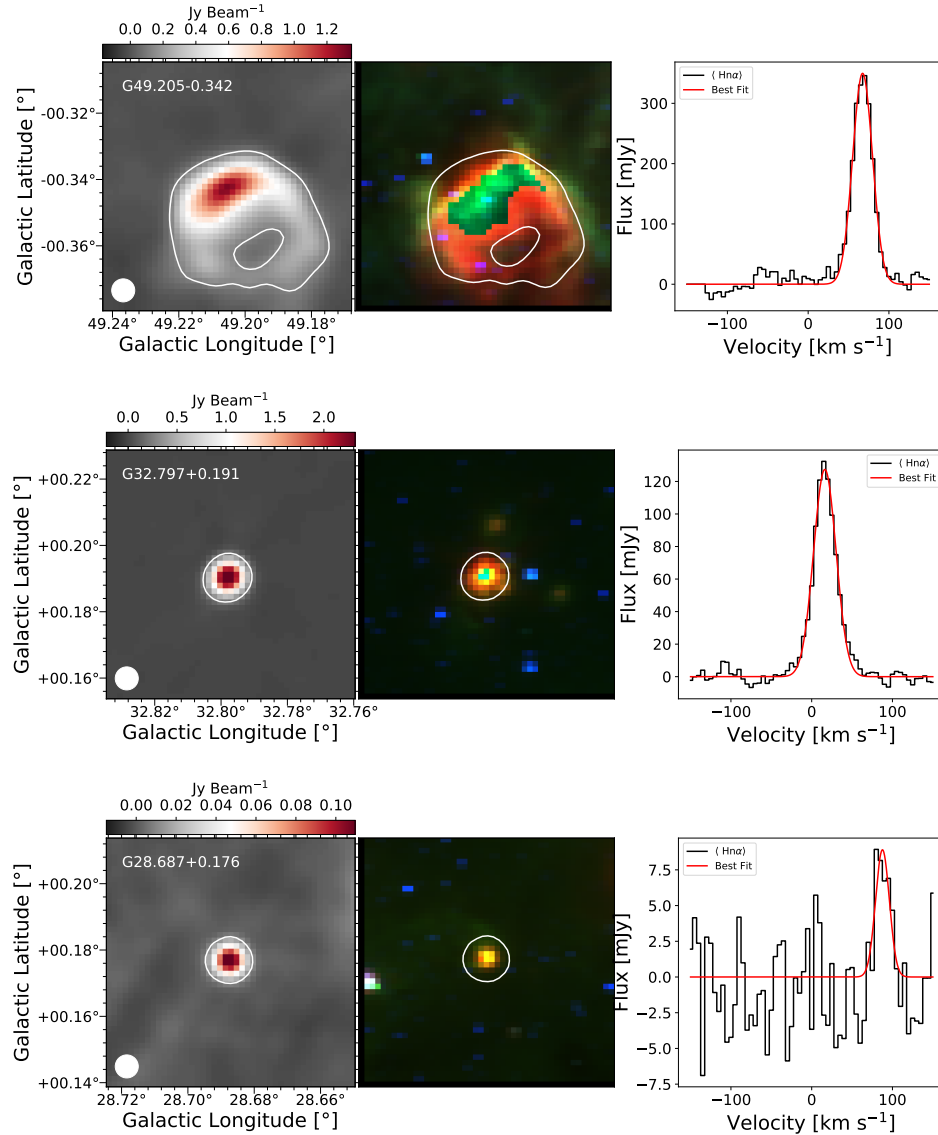
Fig. 1. Examples of three GLOSTAR H II regions. G049.205−0.342 (top panel) and G032.797+0.191 (middle panel) exemplify extended and compact radio H II regions found in our catalog, respectively, while G028.687+0.177 (bottom panel) represents the weakest source within our catalog. From left to right: GLOSTAR VLA 5.3 GHz radio continuum emission, a three-color image constructed from *Spitzer* infrared data: MIPSGAL 24 μm (red), GLIMPSE 8.0 μm (green), and GLIMPSE 3.6 μm (blue), and stacked ⟨Hnα⟩ RRL spectra extracted within the region shown as white contour. The filled white circle shows the 25″ GLOSTAR beam.

from an exact frequency coverage match between the line-free continuum and the RRLs. Furthermore, the loss of sensitivity becomes less significant because we are dealing exclusively with relatively bright sources. Similar to RRLs, we also smoothed line-free continuum images to a common angular resolution of 25″ and averaged all line-free continuum images for the six bands that contain the RRLs. Additionally, after excluding the highest frequency RRL, the central frequency of ⟨Hnα⟩ is 5.3 GHz. For comparisons with the RRLs, one should use the continuum fluxes of H II regions mentioned in the current work. For all other purposes, we recommend using fluxes from Medina et al. (2019, and in prep.).

2.3. Complementary data

In addition to the RRL data, we used data of the 870 μm wavelength sub-millimeter continuum emission collected in the APEX Telescope Large Survey of the Galaxy (ATLASGAL)

with a 19.5″ resolution (Schuller et al. 2009; Contreras et al. 2013; Urquhart et al. 2014) to search for the dust emission associated with the H II regions. To study the MIR morphology of the H II regions, we also made use of 3.6 and 8.0 μm band data from the GLIMPSE survey (Benjamin et al. 2003) and 24.0 μm data from the MIPSGAL survey (Carey et al. 2009), both conducted with the *Spitzer* Space Observatory.

3. Source extraction

As was mentioned in Sect. 2, we used RRL data to identify Galactic H II regions. To accomplish this, a straightforward extraction code can be employed to examine each pixel for the presence of line emission that is brighter than its surroundings. An example of such a code is the source extraction code developed by Nguyen et al. (2022) for cataloging methanol masers in the GLOSTAR survey. However, we noticed that this

method is not effective for detecting weak and broad lines. To address this limitation, we capitalized on the fact that H II regions are bright sources in the radio continuum. Therefore, we began by extracting continuum sources from a line-free continuum image. To create the continuum maps, we imaged the line-free channels (Sect. 2.2). The source extraction process was performed using the BLOBCAT[4] software package, which was developed by Hales et al. (2012). BLOBCAT is a Python script that uses a flood-fill algorithm to detect and identify clusters of pixels representing sources in two-dimensional radio wavelength images. This package has been employed to create source catalogs for various surveys, including the GLOSTAR survey (Medina et al. 2019, 2024; Dzib et al. 2023; Yang et al. 2023) and the HI/OH/Recombination line survey of the inner Milky Way (THOR; Bihr et al. 2016; Wang et al. 2018). We followed the same methodology as Medina et al. (2019), who created a continuum source catalog within the region of $28° \leq \ell \leq 36°$, $|b| \leq 1°$. Since the noise in the GLOSTAR survey is position-dependent, we generated independent noise maps using the SExtractor package[5] (Bertin & Arnouts 1996) from the line-free continuum data. This algorithm assigns a root mean square (rms) value to each pixel in an image by analyzing the distribution of pixel values within a local mesh until all values converge around a chosen σ value.

To perform automatic source extraction, we used the BLOBCAT software with the noise map as input and used a detection threshold (parameter dSNR in BLOBCAT) of four. This process created a catalog of continuum sources along with their corresponding continuum source masks. To identify sources with RRL brightness higher than the surrounding noise, we developed a simple Python code. This code first applies the continuum source mask generated by the BLOBCAT script to the RRL image and extracts the stacked RRL spectra averaged over the blob. For each blob, the script calculates the signal-to-noise ratio for each velocity channel. If three consecutive channels along the spectral axis are found to have a signal-to-noise ratios greater than three times the standard deviation, the source was considered for further examination. Implementing these input parameters led to the detection of 265 continuum sources with associated RRL emission within the studied region.

Due to missing short spacing information, the VLA observations are not sensitive to emission on scales larger than ~120″ in the D (most compact) configuration at ~6.0 GHz. Consequently, some sources that exhibit uniform emission on such large spatial scales may not be detected in the VLA observations. However, the observations are expected to detect clumpy emission within these large H II regions. Therefore, no size restriction was imposed when defining the sample. Nevertheless, the sample may contain spurious detections, such as emission from side lobes and large-scale structures that have been over-resolved, causing the emission to split into multiple components. To address these potential false detections, we cross-referenced the sources with characteristic MIR images and also compared them spatially with the WISE H II region catalog (Anderson et al. 2014). Additionally, we required that the peak amplitude of the ⟨Hnα⟩ RRL signal must be at least three times the local RMS noise around the source in the RRL image. Fig. 2 shows the distributions of the local RMS noise values of the velocity channels around the RRLs and the signal-to-noise ratios of the detected RRLs. A flow chart illustrating the method is presented in the Fig. 3. Using this approach, we created an unbiased catalog of

---
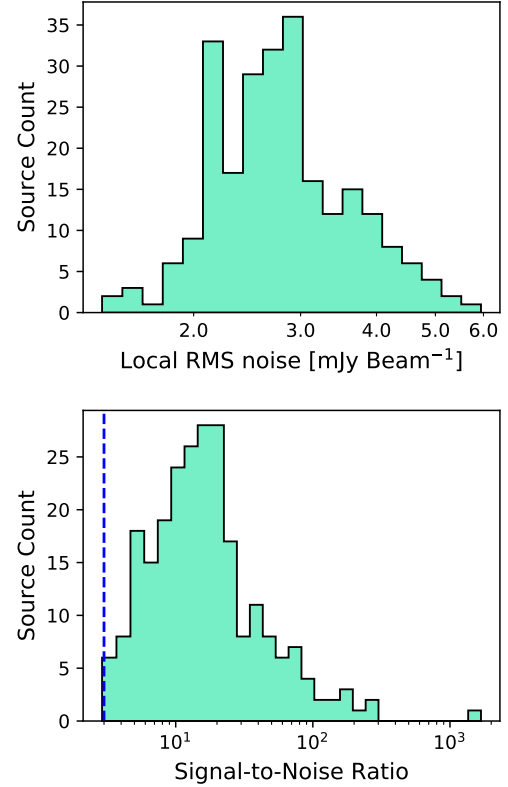
Fig. 2. Histograms of the values of the local RMS noise of the velocity channels around the RRL (top) and the signal-to-noise ratio (bottom) for all the RRLs detected in this study. The median value of RMS noise level is ~3.0 mJy beam^{-1}. The dashed blue line represents the 3σ level.

244 Galactic H II regions based on RRL observations conducted with VLA in the D-configuration.

4. Results

4.1. Source catalog

We identified a total of 244 sources with RRL emission above 3σ (where σ is local rms noise ranging from 1.6 to 6.0 mJy beam^{-1}, with the median of 3.0 mJy beam^{-1}). Among these H II regions, 13 sources are located in the Cygnus X region, and 29 are found toward the Galactic center region within $358° \leq \ell \leq 2°$, $|b| \leq 1°$. Within this subset of 29 H II regions toward the Galactic center, five sources are in the close vicinity of the thermally ionized Arched filament (Lang et al. 2001). In Fig. 4, we show the spatial distribution of the detected H II regions superimposed on the D-configuration continuum image. Fig. 5 displays the Galactic longitude and latitude distribution of the detected sources. Notably, we see peaks in the source distribution at Galactic longitudes corresponding to sites of massive star formation, such as W31, W43, and W51. Along the Galactic latitude, we observe an asymmetric distribution whereby the majority of sources are situated at negative latitudes, as is reported by Anderson et al. (2014). Negative latitudes account for over 61% of all sources, while positive latitudes make up the remaining 39%. Furthermore, a few sources at higher Galactic latitudes ($\ell > 1.0°$) are located in the Cygnus X star-forming region. The mean of this distribution is $b = -0.07 \pm 0.01°$. The cause of this displacement is commonly attributed to the position of the Sun above the actual Galactic mid-plane (Schuller et al. 2009; Anderson et al. 2014, 2019).
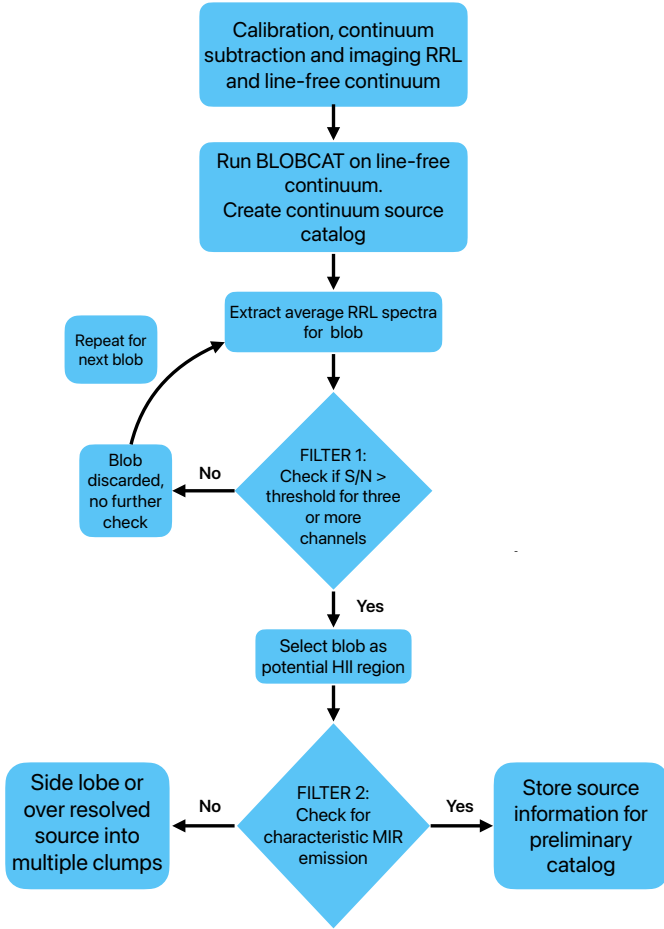
Fig. 3. Flow chart illustration of the source extraction process described in Sect. 3.

Table C.1 presents the continuum flux and $\langle Hn\alpha \rangle$ RRL parameters, accompanied by the distances of H II regions, along with associations with the dust continuum and 6.7 GHz methanol masers (see Sects. 5.2 and 5.3). The Galactic coordinates of the peak continuum emission are listed in Columns 3 and 4, while Columns 5 and 6 display the peak (S_{peak}) and integrated continuum flux density (S_{int}), respectively. For the RRL parameters, Columns 8, 10, and 12 present the amplitude (S_L), full-width half maximum (FWHM) line-width (ΔV), and peak LSR velocity (V_{LSR}), respectively. These values were derived by fitting a Gaussian to the $\langle Hn\alpha \rangle$ RRL. Additionally, Columns 13 and 15 indicate the heliocentric (D_{sun}) and Galactocentric distances (R_{Gal}), respectively (see Sect. 4.2). In Fig. 6, we show the distribution of detected RRL velocity with the Galactic longitude. As is seen in this figure, most sources align with the spiral arm models of Taylor & Cordes (1993) and Reid et al. (2019). Almost no H II regions are detected in the more distant outer arms, which is likely due to the limited sensitivity.

In addition to H II regions, planetary nebulae (PNe) also emit thermal radiation, making them the primary source of contamination in the H II region sample. Planetary nebulae are the expanding circumstellar envelopes of the asymptotic giant branch (AGB) stars that are ionized by their hot central white dwarf remnant. Consequently, RRLs from PNe generally exhibit larger line widths ($\sim$30–50 km s^{-1}) compared to those observed in H II regions. Physically, PNe are smaller than H II regions,

rendering them unresolved and devoid of nebulosity in MIR emission. To ensure the accuracy of our H II region sample, we conducted a matching analysis with the SIMBAD[6] database to exclude any previously known PNe within a radius of 1'. Recently, Dzib et al. (2023) and Yang et al. (2023) identified numerous new PNe candidates in the GLOSTAR regions using high-resolution VLA B-configuration continuum data. However, upon conducting a crossmatch, we did not identify any PNe located within a 25'' radius. Additionally, we employed the characteristic MIR emission to identify any potential contamination from PNe. Our investigation did not reveal any indications of PNe contamination in our H II region sample.

The GLOSTAR survey offers one of the first interferometry blind surveys of RRLs. However, challenges arise in directly comparing radio properties with previous RRL studies due to differences in *uv* coverage, spatial filtering, and angular resolution. Here, our primary objective is to identify common sources with existing H II region surveys. The Green Bank Telescope Galactic H II region discovery survey (HRDS; Bania et al. 2010; Anderson et al. 2011) is a hydrogen RRL emission survey toward previously unknown Galactic H II regions within $-16° \leq \ell \leq 67°$ and $|b| \leq 1°$. In its course, 603 discrete hydrogen RRL components were detected at 9 GHz from 448 targets. The HRDS survey has an angular resolution of 82'', which is much larger than our survey resolution of 25''. Crossmatching by eye, we found only 34 common sources. Kalcheva et al. (2018) present a catalog of 239 UC H II regions found in the Co-Ordinated Radio 'N' Infrared Survey for High-mass star formation survey (CORNISH; Hoare et al. 2012) at 5 GHz and 1.5'' angular resolution in the Galactic region of $10° \leq \ell \leq 65°$ and $|b| \leq 1°$. We crossmatched with CORNISH UC H II regions using a separation threshold of 12'', which is half the GLOSTAR beam size. We find 68 GLOSTAR H II regions associated with 84 CORNISH UC H II regions within 12'' ($\sim$28%), with an average separation of 4'' between the GLOSTAR and CORNISH peaks. Using data from WISE, Anderson et al. (2014) compiled a catalog of over 8000 "known", "candidate", "group", and "radio-quiet" Galactic H II regions. The WISE H II region catalog also includes the HRDS and many other H II region catalogs (e.g., follow-up observations of the HRDS and southern sky survey, SHRDS; Wenger et al. 2021). Within the region covered by GLOSTAR, the most recent version of the WISE catalog reported $\sim$1100 known, $\sim$650 candidates, $\sim$325 groups, and $\sim$1540 radio-quiet. Out of our detected 244 H II regions, 209 are known, 11 are candidates, 20 are groups, and two are radio-quiet H II regions in the WISE H II region catalog. For the sources spatially associated with multiple sources in the WISE H II region catalog, known H II regions were designated preferentially. For the sources that have more than one source within the radius of a cataloged WISE H II region, we assigned them to the same group, whereas for two sources (G028.569+0.020 and G034.322+0.160) we did not find any association with the WISE catalog. Since the RRLs fluxes are generally about 10% of the continuum fluxes and are associated with relatively bright H II regions, we expect most of the detected sources to be previously known.

4.2. Distances

In order to derive the physical properties of the detected H II regions, their distances must be estimated first. This has been

---

[6] https://simbad.cds.unistra.fr/simbad/
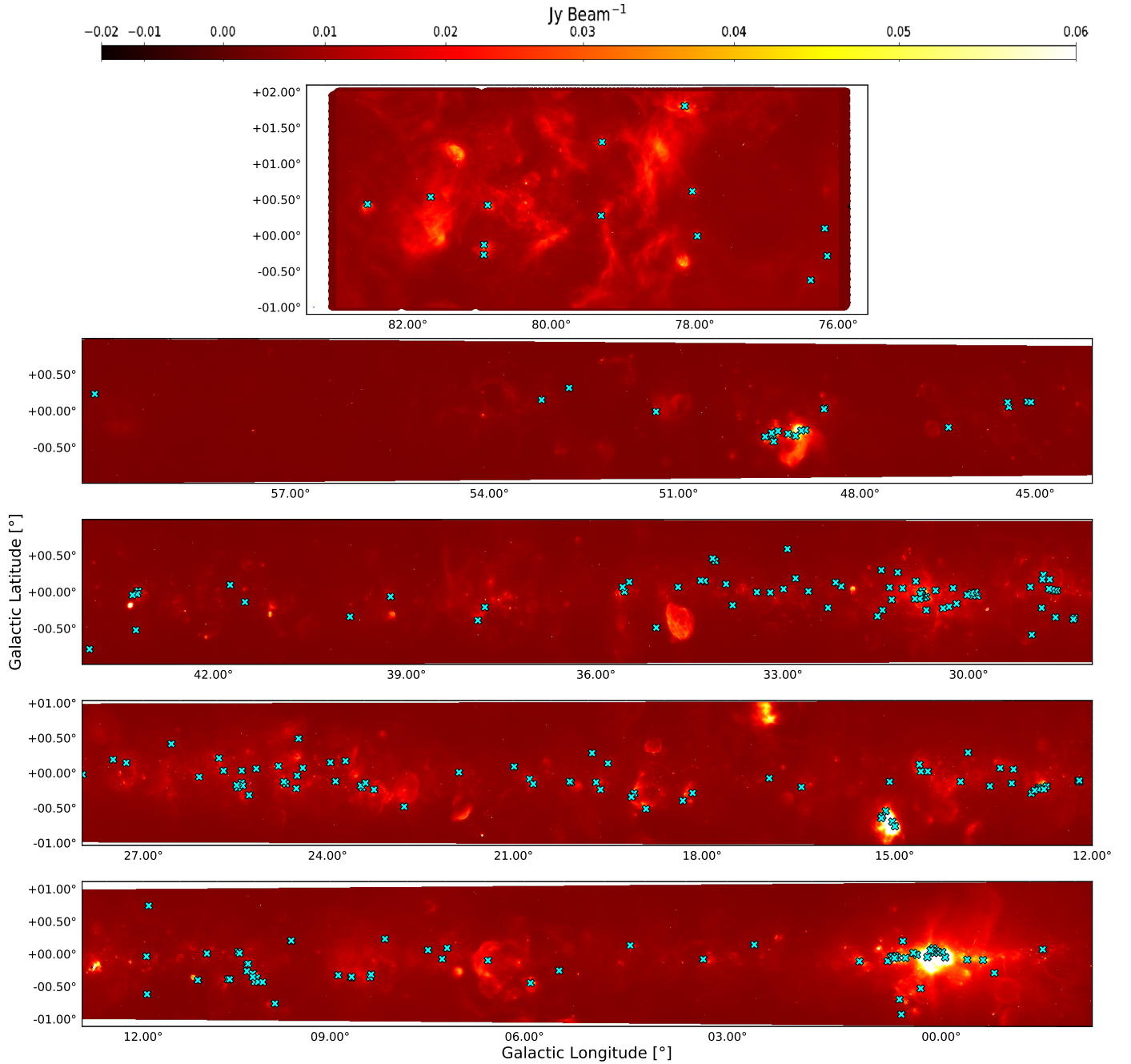
Fig. 4. Detected ⟨Hnα⟩ RRLs plotted as cyan crosses on top of a combination of the VLA D configuration and the Effelsberg 100m single-dish continuum image for the entire GLOSTAR survey region ($-2° \leq \ell \leq 60°$, $|b| \leq 1°$ and Cygnus X region; Medina et al. 2019; Brunthaler et al. 2021). The flux has been limited to between -0.02 and 0.06 Jy beam^{-1} for visibility.

accomplished through a multi-step process, involving the adoption of reliable distances from the literature if available, determination of the kinematic distances to all remaining sources with available RRL velocities, and resolution of any resulting distance ambiguities using the archival H I data. These steps are elaborately described in Appendix A.

Deriving kinematic radial distances toward the Galactic center and Cygnus X regions sparks debate due to the degeneracy of Galactic velocities in the direction of Cygnus X (Galactic longitude close to 90°) and the Galactic center. We have excluded H II regions within a few degrees of the Galactic center (i.e., $358° \leq \ell \leq 3°$) because kinematic distances for sources in this region are highly unreliable. In this study, we include the Galactic center

H II regions in the source catalog (presented in Table C.1) and derive their electron temperatures. We refrain from deriving the remaining physical properties of the Galactic center H II regions due to uncertainty in the kinematic distances toward the Galactic center.

Determining the distances to individual clouds and H II regions in Cygnus X has been a persistent challenge (Schneider et al. 2006). Previous parallax measurements and line-of-sight extinctions suggest that the bulk of molecular gas should be located at 1.3–1.5 kpc in this complex (Rygl et al. 2012; Dzib et al. 2013; Xu et al. 2013; Zucker et al. 2020; Chen et al. 2020a; Dharmawardena et al. 2022). Given that the molecular clouds in Cygnus X are associated with each other
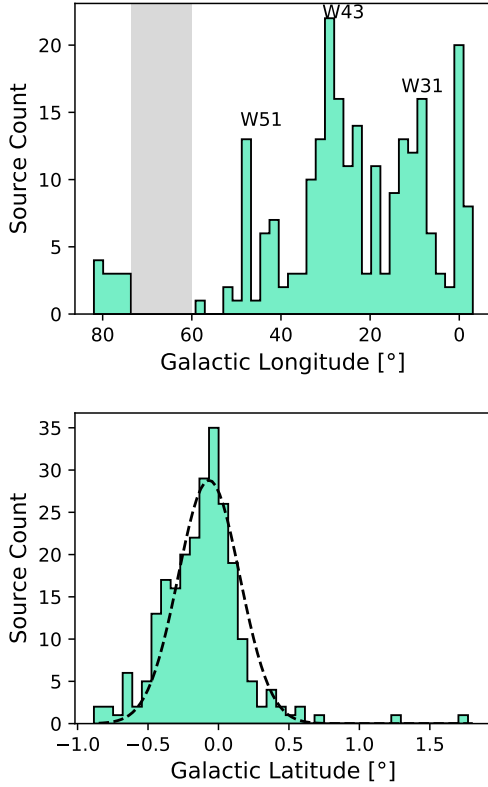
Fig. 5. Top panel: histogram showing the distribution of the GLOSTAR H II region along the Galactic longitude. The bin size used is 2.0° from the $\ell = -2.0°$ to 83°. Bottom panel: histogram showing the distribution along the Galactic latitude with a bin width of 0.07°. The mean of the distribution is $b = -0.07 \pm 0.01°$. The region shaded in gray represents a longitude range of 60° to 76°, which was not included in the GLOSTAR survey.

(Schneider et al. 2006; Gong et al. 2023), we adopted a distance of 1.4 kpc for the Cygnus X H II regions.

Using these steps, we obtained the distances from the literature for 149 sources between $3° \leq \ell \leq 60°$. For the rest of the 53 sources, we solved the kinematic distance ambiguity using the H I emission/absorption (H I E/A) method described by Kolpak et al. (2003), Anderson & Bania (2009), Anderson et al. (2012), and Urquhart et al. (2012), resulting in ~92 % reliable and ~64 % highly reliable distance estimates (see Appendix A for detailed breakdown). In Fig. 7, we show the locations of our H II region sample overlaid on an artistic impression of the Milky Way[7].

4.3. Physical properties of the ionized regions

In this section, we present the physical properties of the cataloged H II regions. Table C.2 lists the various physical properties derived from measurements of their continuum and RRL emission. The first two columns list the effective angular (θ_{source}) and physical (d_{eff}) diameters. Subsequent columns provide the derived electron temperature (T_{e}), EM, electron density (n_{e}), Lyman continuum photon rate (N_{lyc}), ionized gas mass (Mass$_{\mathrm{H\,II}}$), and their corresponding uncertainties. The methodology used to derive these parameters are described in the following sections. Interferometers are insensitive to large scale diffuse emission, such as the nonthermal radio-continuum emission that permeates the Galactic plane. However, they are well

suited for more precise measurements of the total continuum flux density of nebulae, especially when the source's angular size is smaller than the largest angular scale detectable by the telescope. Notably, interferometers like the VLA can simultaneously measure both radio-continuum and RRL emission. This allows precise determinations of the RRL-to-continuum flux ratio that avoid systematic calibration or weather-related issues, bolstering our confidence in the derived physical properties of the H II regions. In the following sections, the detailed processes used to derive these physical properties are discussed.

4.3.1. ⟨Hnα⟩ amplitude and continuum flux density

To obtain a precise line-to-continuum ratio, it is necessary to extract both line and continuum data over the same area of a source. Additionally, the measured line-to-continuum ratio may be influenced by diffuse background emission around the sources. This especially applies to extended objects and H II regions in crowded star-forming regions in the Galactic plane. Given the sensitivity and *uv* coverage of our RRL observations, we did not anticipate any detections toward the weak diffuse thermal emission and certainly not the nonthermal Galactic background. For these reasons, we first performed background subtraction and then manually determined the continuum flux and generated the ⟨Hnα⟩ line profile over the same area of the sources. The mean background intensity ($\overline{\mathrm{B}}$) in the surrounding regions has been estimated using an iterative sigma-clipping algorithm (Dokara et al. 2021, 2023). However, except for a few sources toward the Galactic center, we found that the relative intensity of the background is lower than 1% of peak emission. To determine the continuum flux and generate the ⟨Hnα⟩ line profile over a common area, we began by extracting the line within the range of 10% to 90% of the continuum peak emission. We skipped the peak emission to improve the signal-to-noise ratio by spatially averaging the emission and to calculate the angular area of the H II region. We selected the region with the highest signal-to-noise ratio for the line. This allowed us to generate the average ⟨Hnα⟩ line spectra and determine the continuum flux density of the H II regions. Fig. 8 (top middle panel) displays the distribution of the line amplitudes. Among the H II regions in our catalog, the brightest one is G015.035–0.677 (M17) with a ⟨Hnα⟩ amplitude of 7.6 Jy, while the weakest is G028.687+0.176 with a ⟨Hnα⟩ amplitude of 8 mJy. The mean and median values of the amplitude distribution are 0.11 Jy and 0.04 Jy, respectively. We utilized the line-free channels to determine the continuum flux density (S_{C}). This was done by integrating over the same area as that used to generate the line profile. Hence, the continuum flux density derived here will be lower than that obtained by integrating over the entire source. We estimated S_{C} as

$$S_{\mathrm{C}} = \left(\sum_{i=1}^{N_{\mathrm{src}}} A_i - N_{\mathrm{src}} \overline{B} \right) \times a_{\mathrm{bm}}^{-1}, \tag{1}$$

where $\sum_{i=1}^{N_{\mathrm{src}}} A_i$ is the total intensity summed over the N_{src} pixels, $\overline{B}$ is the mean background intensity, and $a_{\mathrm{bm}} = \pi \theta_{\mathrm{bm}}^2 / (4\ln(2)\Delta_{\mathrm{pixel}}^2)$ is the number of pixels per beam, where $\Delta_{\mathrm{pixel}}^2$ is the area of each pixel. To accommodate the uncertainty in flux estimation, we incorporated a GLOSTAR flux density calibration error of 5%. The top left panel of Fig. 8 illustrates the distribution of continuum flux density (S_{C}). Within our catalog, the H II region G015.035–0.677 (M17) is the brightest, with a continuum flux

---

[7] https://photojournal.jpl.nasa.gov/catalog/PIA19341
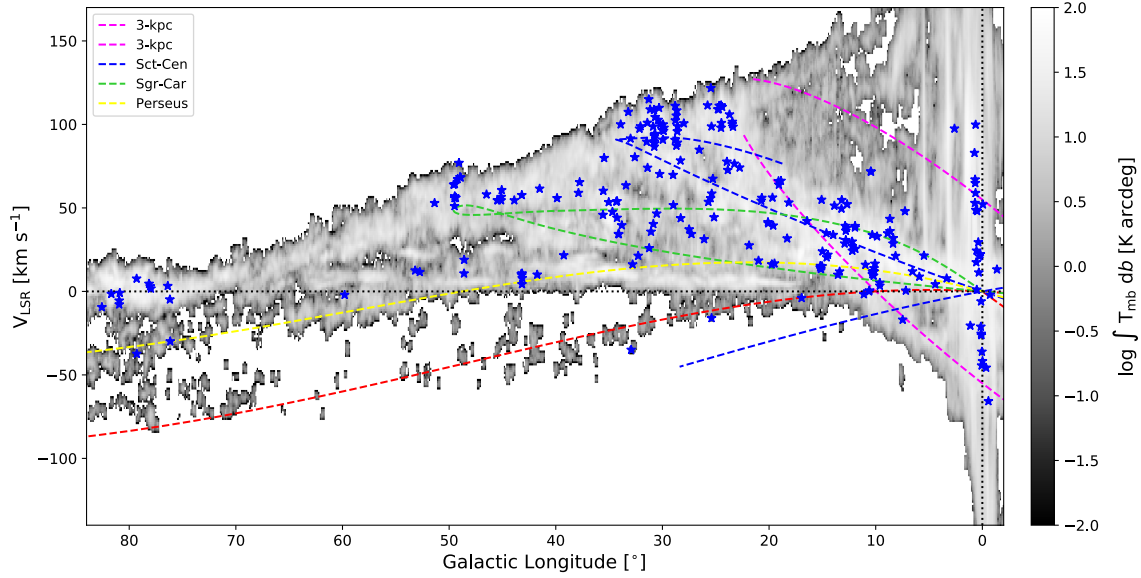
Fig. 6. Distribution of detected H II regions RRL peak velocity with respect to the Galactic longitude in blue stars. The dashed lines represent the updated spiral arm models of Taylor & Cordes (1993). The background shows the CO emission from Dame et al. (2001).
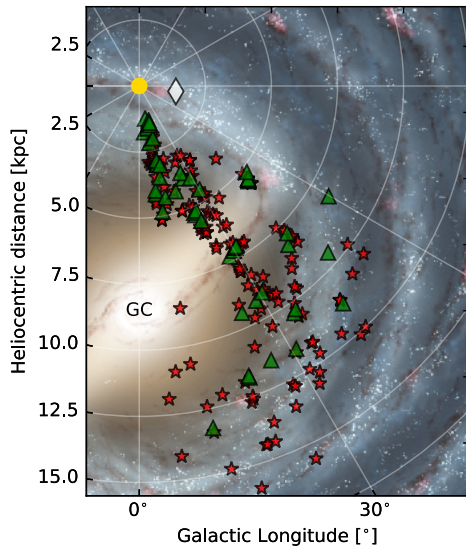
Fig. 7. Distances of H II region from GLOSTAR D-configuration VLA observations plotted on top of an artist's rendition of the Milky Way. The red stars represent the positions of H II regions with distances adopted from the literature, while the green triangles represent H II regions for which we derived the kinematic distances (see text for details). We adopt a distance of 1.4 kpc for Cygnus X H II regions represented by white diamond.

density of 185.6 Jy, while G025.479–0.174 stands out as the weakest, with a continuum flux density of 0.037 Jy. The mean and median values of the S_C distribution are 2.36 Jy and 0.62 Jy, respectively. The angular diameters of the H II regions are determined from the number of pixels within the same area of the source used to generate the line profile, $\theta_{source} = 2\sqrt{\frac{N_{src}\Delta_{pixel}^2}{\pi}}$.

4.3.2. Line widths

Fig. 8 (top right panel) shows the distribution of the FWHM line widths of the detected ⟨Hnα⟩ RRLs. The mean ± standard deviation of this distribution is 28.2 ± 10.2 km s^{-1}, respectively.

Notably, our sample exhibits a comparable, if slightly broader FWHM distribution compared to that of the HRDS (Anderson et al. 2011), Lockman (1989) and Chen et al. (2020b), which are 22.3 ± 5.3, 26.4 ± 8.1, and 23.6 ± 2.0 km s^{-1}, respectively. These differences in FWHM may be attributed to the difference in spectral resolution used in the respective studies, which are 5.0, 1.86, 4.0, and 0.4–2.4 km s^{-1} for the GLOSTAR survey, the HRDS (Anderson et al. 2011), Lockman (1989), and Chen et al. (2020b).

We detected 40 H II regions with RRL width >35 km s^{-1}. Of these sources, 13 sources are found in the Galactic center region ($-2° \leq \ell \leq 2°$ and $|b| \leq 1°$) and two toward the Cygnus X region ($76° \leq \ell \leq 83°$, $-1° \leq b \leq 2°$). Anderson et al. (2011) propose that line widths greater than 35 km s^{-1} should be viewed with caution as they could be due to low signal-to-noise detection, the presence of blended velocity components, or an indication that the source is not an H II region. As the spectral signal-to-noise ratio decreases, the process of Gaussian fitting for deriving the line width becomes increasingly uncertain. In situations with low signal-to-noise, it may become challenging to separate double-velocity components, potentially resulting in an erroneously large line width estimation. In Fig. 9, we plot the line width as a function of the line intensity. The plot demonstrates that the RRL amplitude distribution for the broad RRL H II regions resembles the overall distribution. Within our sample of 40 broad RRL H II regions, 31 sources have signal-to-noise ratios greater than 10σ. This suggests that the broad line widths we determine for RRL H II regions in our sample are not due to a low signal-to-noise ratio.

The line widths of the RRLs can be influenced by a blend of thermal, turbulent, and organized motions, such as those arising from processes like accretion dynamics, infall of matter, and outflow. For typical H II regions with electron temperatures of approximately ∼10^4 K, the thermally broadened line width is about 25 km s^{-1}. However, the RRLs line widths of Galactic H II regions can exceed this, indicating that they are significantly influenced by turbulent and ordered motions. In addition, pressure broadening is also significant for RRLs at centimeter wavelengths (Keto et al. 2008). Young and compact H II regions can show broadened (>40 km s^{-1}) RRLs (Sewilo et al. 2004;
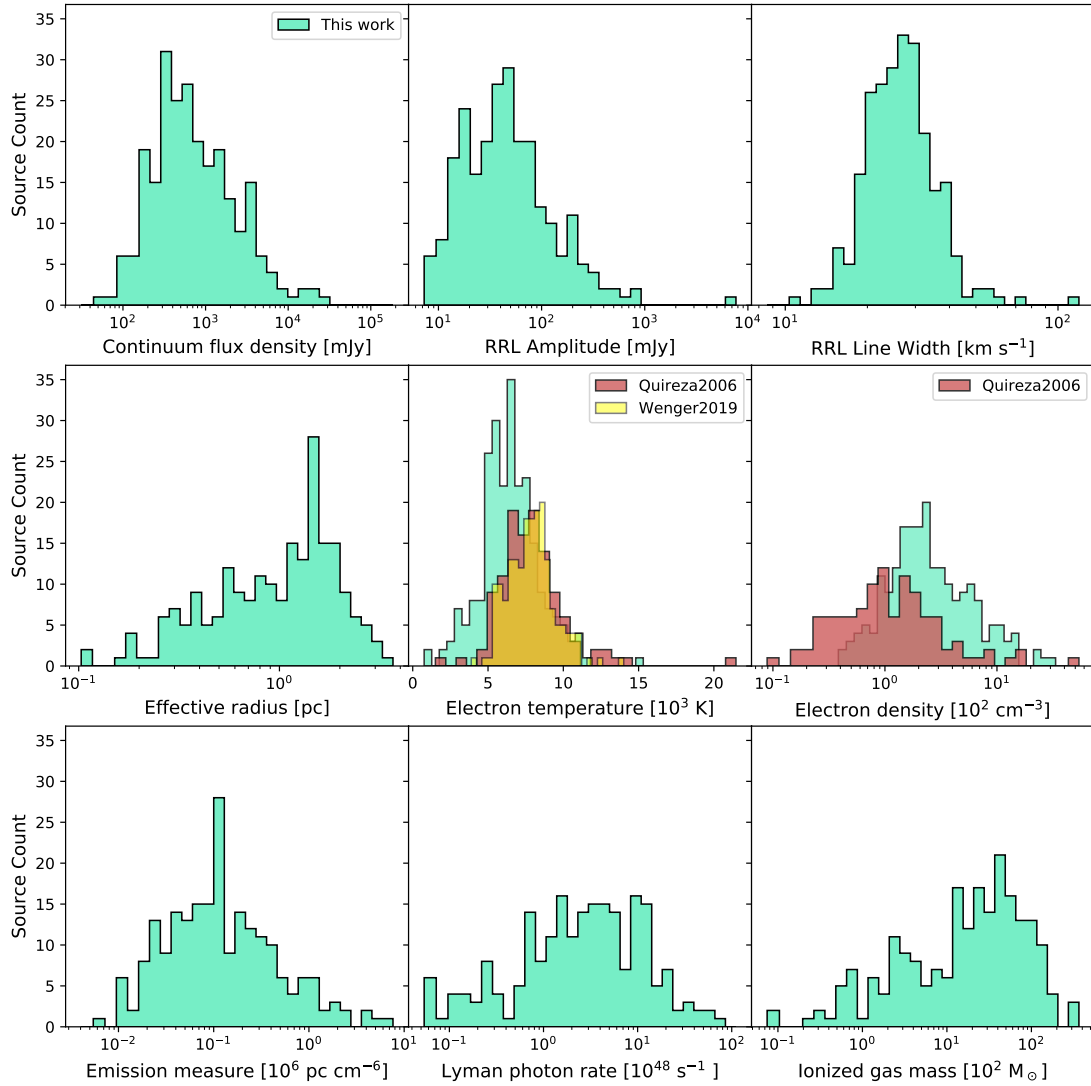
Fig. 8. Distributions of various H II region physical properties from top left to bottom right, continuum flux density, RRL amplitude, RRL FWHM, effective radius, electron temperature, electron density, EM, Lyman photon rate, and ionized gas mass. The electron temperature reported by Quireza et al. (2006) is indicated in red, while the one reported by Wenger et al. (2019) is shown in yellow, and these are compared to the GLOSTAR H II region sample (aquamarine). On average, the electron temperature of GLOSTAR H II regions (6707 K) is lower than that of Quireza et al. (2006) (8214 K) and Wenger et al. (2019) (8055 K). Electron density histograms are presented for both the GLOSTAR (aquamarine) and Quireza et al. (2006) (red) H II region samples. On average, the GLOSTAR nebulae have higher electron density than the Quireza et al. (2006) sources.

Keto et al. 2008) due to the presence of large-scale motion of ionized gas around a young central star. However, it is not yet confirmed that the broad RRL is an intrinsic property of HC H II regions. Yang et al. (2019) compiled a catalog of 120 candidate HC H II regions located in the Galactic plane region within $10° \leq \ell \leq 65°$ and $|b| \leq 1°$. In the region overlapping with the GLOSTAR survey coverage ($10° \leq \ell \leq 60°$ and $|b| \leq 1°$), we detected 23 H II regions with RRL widths exceeding 35 km s^{-1}. To establish associations with the candidate HCH II regions from Yang et al. (2019), we performed a crossmatch using a distance threshold of 12″, half of the GLOSTAR beam size. As a result, we identified 15 (out of 23) broad RRL H II regions that are associated with the candidate HC H II regions, with a mean ± standard deviation separation of 3.3 ± 1.3″. Furthermore, the mean ± standard deviation of the spectral indices between 1.4–5 GHz for these 15 broad RRL H II regions as reported by Yang et al. (2019) is 0.6 ± 0.3. Hence, these 15 broad RRL H II regions are very likely to be HC H II regions.

Our catalog has only 4 (2%) H II regions with extremely narrow line widths (<15 km s^{-1}). Narrow RRL widths are interpreted to be purely thermal, originating from "cool" nebulae with electron temperatures $\lesssim 5000$ K. Anderson et al. (2011) showed that cold nebulae are very rare in our Galaxy; only 6% of HRDS sources have line widths smaller than 15 km s^{-1}. However, this fraction is three times higher than that found in our survey. This can be attributed to the poorer spectral resolution of our RRL data along with our selection criteria, which rejected sources emitting in only two channels, making the detection of narrower lines more challenging.

4.3.3. Local thermal equilibrium electron temperatures

The detection of RRLs allows us to calculate the electron temperature of the ionized gas. The electron temperature of a nebula is obtained from the RRL-to-continuum ratio, $S_{\mathrm{L}}/S_{\mathrm{C}}$. Since we wanted to derive the average electron temperature, we assumed

Table 2. Candidate HC H II regions.

S.No.	GLOSTAR name	CORNISH name	Separation [*] (″)	ΔV (km s^{-1})	α [**]	d_{eff} [***] (pc)
1	G010.624–0.384	G010.6234–00.3837	2.43	38.69 ± 1.6	0.97	1.24
2	G010.302–0.147	G010.3009–00.1477	4.75	38.36 ± 1.79	0.31	0.78
3	G011.937–0.615	G011.9368–00.6158	2.89	40.52 ± 1.89	0.36	0.71
4	G012.805–0.200	G012.8050–00.2007	2.41	37.63 ± 0.5	0.84	0.88
5	G013.210–0.144	G013.2099–00.1428	4.3	36.39 ± 1.72	0.61	1.15
6	G016.944–0.074	G016.9445–00.0738	1.92	43.81 ± 4.64	0.55	3.65
7	G026.544+0.415	G026.5444+00.4169	6.96	36.92 ± 2.5	0.25	3.74
8	G028.287–0.364	G028.2879–00.3641	3.22	39.27 ± 5.38	0.23	0.7
9	G029.957–0.017	G029.9559–00.0168	4.22	39.92 ± 1.33	0.52	1.31
10	G030.535+0.021	G030.5353+00.0204	2.42	36.77 ± 1.76	0.2	3.05
11	G034.257+0.153	G034.2572+00.1535	2.06	59.79 ± 2.6	1.22	0.77
12	G037.874–0.399	G037.8731–00.3996	3.97	43.73 ± 1.59	0.55	2.59
13	G043.165–0.029	G043.1651–00.0283	2.62	40.06 ± 1.16	1.23	1.93
14	G045.122+0.131	G045.1223+00.1321	4.0	57.83 ± 1.64	0.63	1.47
15	G049.490–0.369	G049.4905–00.3688	2.03	38.4 ± 0.83	0.93	0.61

Notes. [*]Angular separation between GLOSTAR and CORNISH peak emission. [**]Spectral index between 1.4–5 GHz as reported by Yang et al. (2019). [***]d_{eff} represents the effective diameter of the source (refer to Sect. 4.3.2), and these values might exceed the true size of the sources.
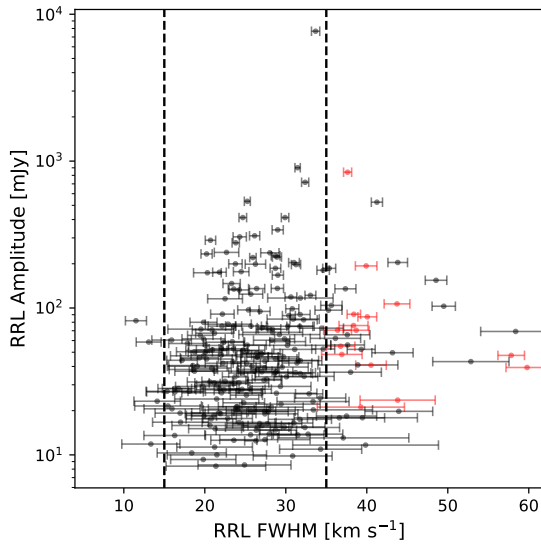
Fig. 9. H II region's RRL intensity as a function of FWHM line width. Vertical dashed lines represent the line width of 35 and 15 km s^{-1}. The distribution of the low intensity sources is similar to the entire source. The candidate HC H II regions are represented by the filled red circle.

all sources to be homogeneous, isothermal, and their continuum emission to be optically thin at the GLOSTAR frequency (5.3 GHz). However, this last assumption is not true for candidate HC H II regions (see Table 2), which have a positive spectral index (up to 2) between 1.4 and 5 GHz. We lack the information of the turn-over frequency for these regions, when the emission becomes optically thin. Therefore, accurately estimating the actual optical depth at 5.3 GHz becomes challenging. Consequently, the true electron temperature is likely to be lower than what we derive from our assumption of optically thin continuum emission. In Table C.2, we indicate these sources with (*) for the reader's reference. When the radio continuum emission is optically thin, one can estimate the electron temperature using the

following equation (see, e.g., Wenger et al. 2019):

$$\left(\frac{T_e}{K}\right) = \left\{ 3.661 \times 10^4 \frac{\Delta n}{n} f_{\mathrm{nm}} \left(\frac{\nu}{\mathrm{GHz}}\right)^{1.1} \left(\frac{S_C}{S_L}\right) \left(\frac{\Delta v}{\mathrm{km\,s^{-1}}}\right)^{-1} \right.$$
$$\left. \left[1 + \frac{n(^4\mathrm{He}^+)}{n(\mathrm{H}^+)}\right]^{-1} \right\}^{0.87}, \tag{2}$$

where Δv is the FWHM line width and $n(^4\mathrm{He}^+)/n(\mathrm{H}^+)$ is the ionic abundance ratio and the expression f_{nm} is the absorption oscillator strength, for which an approximation is given by (Menzel 1968):

$$f_{\mathrm{nm}} = n M_{\Delta n} \left(1 + 1.5 \frac{\Delta n}{n}\right). \tag{3}$$

The expression $\frac{\Delta n}{n} f_{\mathrm{nm}}$ is not a strong function of n for $\Delta n = 1$ hydrogen RRLs. For example, $(\frac{\Delta n}{n} f_{\mathrm{nm}}) = 0.1937$ and 0.1933 for $\Delta n = 1$ and $n = 98$ and 114, respectively, obtained using the oscillator strength from Menzel (1968). Since this variation amounts to only about 0.2% across these H$n\alpha$ transitions, we adopted $(\frac{\Delta n}{n} f_{\mathrm{nm}}) = 0.19345$ for $\Delta n = 1$ and $n = 107$, which is the average of observed principal quantum numbers. After substitution, the final expression for the electron temperature is given by

$$\left(\frac{T_e}{K}\right) = \left\{ 7082.2 \left(\frac{\nu}{\mathrm{GHz}}\right)^{1.1} \left(\frac{S_C}{S_L}\right) \left(\frac{\Delta v}{\mathrm{km\,s^{-1}}}\right)^{-1} \left[1 + \frac{n(^4\mathrm{He}^+)}{n(\mathrm{H}^+)}\right]^{-1} \right\}^{0.87}.$$

We detected helium RRLs only in a few bright sources, so we assume the ionic abundance ratio to be a constant value of 0.07 ± 0.02 (Quireza et al. 2006).

The errors in the electron temperature (σ_{T_e}) were computed by propagating the errors from Gaussian fitting for the line and continuum estimation. To calculate the uncertainty in the derived physical parameters, we utilized the SOERP[8] Python package. SOERP is a Python version of the

---
[8] https://github.com/tisimst/soerp

original Fortran code SOERP, which applies a second-order analysis for error propagation or uncertainty analysis. The electron temperature uncertainty (σ_{T_e}) ranges from 5% to 45%, with a mean of 13% and a standard deviation of 8%. For six sources, G000.121+0.043, G020.098–0.122, G025.459–0.210, G028.687+0.176, G028.789+0.243, and G030.789–0.100, σ_{T_e} exceeds 30%. For G020.098–0.122, G025.459–0.210, G028.687+0.176, G028.789+0.243, and G030.789–0.100, the high uncertainty is attributed to the low line intensity, resulting in increased uncertainty in the obtained amplitude and line-width. The high uncertainty for G0.121+0.043 is a consequence of a weak line and crowded continuum emission around this Galactic center region sources. Fig. 8 (middle center panel) displays the distribution of the derived electron temperature, which has a mean of 6707 K and a standard deviation of 1974 K. G025.479–0.174 and G359.945–0.014 exhibit the minimum (1010±229 K) and maximum (15562±1119 K) electron temperatures, respectively. The elevated electron temperature in G359.945–0.014 can be attributed to contamination by nonthermal continuum emission toward the Galactic center.

In the Galactic center region, the continuum emission is comprised of a significant amount of nonthermal emission in addition to thermal free-free emission (Law et al. 2008; Lang et al. 1997, 2001). Mezger et al. (1996) determined that thermal or nonthermal emission contributed almost evenly within an area of approximately ~400 pc × 350 pc at 5 GHz toward the Galactic center. Among this region, the free-free flux density was measured to be 580 Jy, with 40% originating from radio H II regions and the remainder from extended low-density H II regions. Consequently, we expect depressed values of the line-to-continuum ratio because there is no RRL emission from nonthermal sources. This could lead to a potential overestimation of the reported electron temperature for H II regions in the Galactic center region. A comprehensive analysis of the proportion between thermal and nonthermal emissions is crucial to accurately determine the electron temperature of H II regions toward the Galactic center.

Accurate calculation of electron temperature requires the incorporation of non-LTE (local thermal equilibrium) effects such as stimulated emission, and pressure broadening from electron impact. These non-LTE effects depend on the local density and H II region geometry. However, previous studies (Shaver 1980; Quireza et al. 2006) showed that under many conditions LTE is a good approximation and that the non-LTE electron temperature, T_e^*, is similar to the LTE electron temperature, T_e. Shaver (1980) defines an RRL observing frequency, ν_{LTE}, for which $T_e^* = T_e$. This optimal frequency is a function of EM: ν_{LTE} ~0.081 $EM^{0.36}$. This is independent of the geometry, density, and temperature structure of the H II region. Using our highly reliable values of the EM, we obtain an average frequency of ν_{LTE} = 8.8 GHz. This value is quite close to our observation frequency of 5.3 GHz. Additionally, Wang et al. (2023) demonstrate that the assumption of LTE to calculate T_e is not valid for the transitions they observed in L band (1–2 GHz), and hence, non-LTE corrections are needed. However, the necessity for non-LTE corrections is insignificant for X and C bands (including the range covered by the GLOSTAR survey). We therefore conclude that our estimated LTE electron temperatures are close to the real electron temperatures of the H II regions we detect.

Despite the significant difference in beam size, we attempted to identify common sources by performing a crossmatch within a threshold distance of 25″ (GLOSTAR beam size) with Quireza et al. (2006) and Wenger et al. (2019). The average percentage difference between our electron temperature and those of

Quireza et al. (2006) and Wenger et al. (2019), for the common sources are 1.0% and 4%, respectively. In Fig. 8 (middle center panel), we compare the distributions of electron temperature. A systematic variation in the T_e values is evident. There are several possible explanations for the origin of this difference. As pointed out by Quireza et al. (2006), RRL studies were conducted at various frequencies, utilizing different telescopes that have distinct beam sizes. Consequently, each survey investigates different regions within the nebulae. Furthermore, certain H II regions exhibit intricate internal structure characterized by significant density and temperature fluctuations. When deriving electron temperatures from different RRL transitions observed with diverse telescopes, differences are likely to arise, particularly when assuming LTE. Calibration discrepancies between line and continuum measurements, as well as variations between telescopes, may also introduce additional challenges. For example, the FWHM of 3′.20 at 8.6 GHz in Quireza et al. (2006) was much larger than ours leading to them observing more extended gas compared to our observations, which is reflected in the distribution of electron density in Fig. 8 (middle right panel). All things being equal, we expect higher electron density to produce higher electron temperature because the electron density affects the rate of collisional de-excitation. Hence, a high value of n_e inhibits cooling, and thus increases the T_e (Rubin 1985). However, in Fig. 8 (middle center and right panel), we observe the opposite: the GLOSTAR H II region distribution shows higher n_e but lower T_e compared to Quireza et al. (2006). Quireza et al. (2006) assumed H II regions to be homogeneous and spherical, deriving the rms electron density using the peak continuum brightness temperature. The rms densities are probably lower than the true densities of the H II regions since generally the gas is not homogeneously distributed, showing a hierarchical structure, as was discussed in Yang et al. (2019). Additionally, the metallicity, which is a function of R_{Gal}, primarily regulates the electron temperature. Therefore, a detailed study is required to understand these differences.

4.3.4. Emission measure, electron density, Lyman photon rate, and ionized mass

Knowing the angular size and distance of the H II regions we can estimate further physical properties of the H II regions. Considering H II regions as fully ionized Strömgren spheres without dust and assuming optically thin emission, the relation between EM and flux density is given by Schmiedeke et al. (2016):

$$\left(\frac{S_\nu}{Jy}\right) = 2.525 \times 10^{-2} \left(\frac{T_e}{K}\right)^{-0.35} \left(\frac{\nu}{GHz}\right)^{-0.1} \left(\frac{EM}{pc\ cm^{-6}}\right) \Omega_{source} \quad (4)$$

where Ω_{source} is the solid angle of the source. The EM for a circular aperture is given by Schmiedeke et al. (2016):

$$\left(\frac{EM}{pc\ cm^{-6}}\right) = 3.217 \times 10^7 \left(\frac{S_\nu}{Jy}\right) \left(\frac{T_e}{K}\right)^{0.35} \left(\frac{\nu}{GHz}\right)^{0.1} \left(\frac{\theta_{source}}{arcsec}\right)^{-2}. \quad (5)$$

From this, we can get this expression for the electron density (n_e),

$$\left(\frac{n_e}{cm^{-3}}\right) = 2.576 \times 10^6 \left(\frac{S_\nu}{Jy}\right)^{0.5} \left(\frac{T_e}{K}\right)^{0.175} \left(\frac{\nu}{GHz}\right)^{0.05}$$
$$\left(\frac{\theta_{source}}{arcsec}\right)^{-1.5} \left(\frac{D}{pc}\right)^{-0.5} \quad (6)$$

where F_ν is the flux density at frequency ν, D is the distance to the source, T_e is the electron temperature, and θ_{source} is the effective angular diameter of the ionized region. Similarly, the expression for the Lyman photon rate of an H II region is taken from Schmiedeke et al. (2016),

$$\left(\frac{N_{Lyc}}{s^{-1}}\right) = 4.771 \times 10^{42} \left(\frac{S_\nu}{Jy}\right) \left(\frac{T_e}{K}\right)^{-0.45} \left(\frac{\nu}{GHz}\right)^{0.1} \left(\frac{D}{pc}\right)^2. \quad (7)$$

Finally, following Tielens (2005), we can estimate the ionized mass of the H II regions using the following equation,

$$\frac{M_{H II}}{M_\odot} = 80 \times \left(\frac{10^3 \, cm^{-3}}{n_e}\right) \left(\frac{N_{Lyc}}{5 \times 10^{49} \, s^{-1}}\right). \quad (8)$$

Fig. 8, shows the distribution of the EM, electron density (n_e), Lyman photon rate (N_{Lyc}) and ionized gas mass ($M_{H II}$). The median of EM, n_e, N_{Lyc}, and $M_{H II}$ of our sample are 1.1×10^5 pc cm^{-6}, 2.5×10^2 cm^{-3}, 2.3×10^{48} s^{-1} and $14.5 \, M_\odot$, respectively. The distribution of N_{Lyc} ranges from 3.8×10^{46} s^{-1} to 1.1×10^{50} s^{-1}, corresponding to spectral types of zero-age main sequence (ZAMS) stars spanning from B0 to O4, assuming that all the ionizing radiation comes from a single star (Martins et al. 2005). Additionally, the ranges of the EM and n_e distributions are 4.7×10^3 to 7.6×10^6 pc cm^{-6} and 0.47×10^2 to 32.0×10^2 cm^{-3}, respectively.

Fig. 10 demonstrates a strong correlation between n_e and the H II region diameter ($r = -0.92$ and p-value $\ll 0.0013$). A least-squares fit to the data results in a power-law exponent of -1.27 ± 0.02, which is consistent with the findings of Kim et al. (2017). Upon comparing the distribution of n_e and the diameter of GLOSTAR H II regions to the typical values for HC H II regions (dashed red lines) and UC H II regions (dashed black lines), we find that our regions are more evolved than UC H II regions. The spatial resolution of the GLOSTAR D-configuration RRL image is 25″, which corresponds to 0.1 pc at a distance of 1 kpc and 0.6 pc at a distance of 5 kpc. Hence, this resolution is insufficient to resolve UC/HC H II regions. However, it is worth noting that some compact H II regions in our survey remain unresolved and show a crossmatch with candidate HC H II regions cataloged by Yang et al. (2019) (see Sect. 4.3.2). This indicates that while our resolution limits our ability to study the smallest H II regions in detail, we still capture some candidate HC H II regions based on spatial correlation and RRL width. To overcome these limitations, the GLOSTAR survey also includes high-resolution observations with the VLA in B-configuration, which will help us detect and study H II regions in their early stages. This approach has been validated by Dzib et al. (2023) and Yang et al. (2023), who discovered many new candidate HC H II regions using the VLA B-configuration continuum data. Additionally, we plan to present a catalog of diffuse H II regions using Effelsberg 100 m observations in the future. With these capabilities, the GLOSTAR survey can study a wide range of H II regions based on their size and evolutionary stages.

In the following sections, we discuss the association of GLOSTAR H II regions with GLIMPSE 8 μm morphology and study the statistical distribution of the physical properties of H II regions with different morphologies. Later sections will explore the association of GLOSTAR H II regions with dust emission and methanol masers. Since our detected H II regions are evolved (Fig. 10), we do not expect them to be deeply embedded. However, investigating these associations will help us understand the statistical differences in the physical properties of H II regions. Finally, we discuss the Galactic electron temperature gradient.
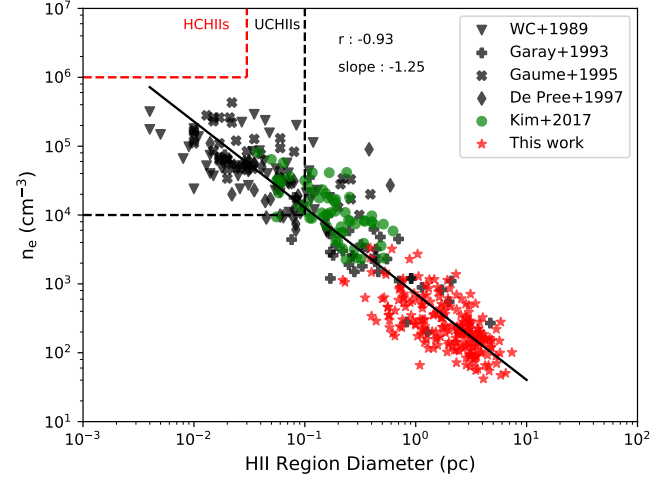

Fig. 10. Electron density (n_e) as a function of H II region diameter (continuation of Fig. 16 of Kim et al. 2017). Black symbols indicate values determined in previous radio continuum surveys and green circles shows the distribution found for a sample of mm-RRLs by Kim et al. (2017), for which the electron densities are derived from mm-RRL emission. The data from the current work are represented by red stars. The solid black lines represent the best-fit line determined by least-square fit to all data with a Spearman's rank coefficient of $r = -0.92$ and p-value $\ll 0.0013$. The dashed red line represents HC H II regions parameter space with diameter ≤ 0.03 pc and $n_e \geq 10^5$ cm^{-3} and the dashed black line represents UC H II regions parameter space with diameter ≤ 0.1 pc and $n_e \geq 10^4$ cm^{-3} (Kurtz et al. 2000).

5. Discussion

5.1. Infrared bubbles

Many sources identified as "bubbles" in the *Spitzer* GLIMPSE data appear to represent H II regions (e.g., Bania et al. 2010; Deharveng et al. 2010; Anderson et al. 2011). To investigate their infrared morphologies, we visually examined the *Spitzer*/GLIMPSE images associated with our RRL sources. Following Anderson et al. (2011), we categorized the 8 μm emissions from GLIMPSE as follows: B – Bubble, featuring 8 μm emission surrounding 24 μm; BB – Bipolar Bubble, consisting of two connected bubbles with a region of strong infrared emission; PB – Partial Bubble, similar to a bubble but incomplete; IB – Irregular Bubble, lacking a well-defined structure; C – Compact, exhibiting compact 8 μm emission; I – Irregular Structure, displaying complex morphology that cannot be easily classified; and ND – Not Detected, indicating either a lack of 8 μm emission or extremely weak emission. Upon analyzing the infrared morphologies, we discovered that approximately 48% (117) of our nebulae exhibit bubble morphology, while 17% (42) appeared compact, and 31% displayed irregular shapes. The remaining 9 sources were classified as 'ND' due to their weak or absent infrared emission. These numbers are summarized in Table 3. Fig. 11 displays MIR images depicting different morphological classifications of sampled GLOSTAR H II regions. Since we utilized an interferometer, our RRL images were not sensitive large scale H II region emission. If RRLs were detected near the periphery of a bubble, we classified its infrared morphology as a bubble. Among the categorized bubble sources, 29% (34 out of 117) had RRLs detected at the edge, while 70% (82 out of 117) had RRLs detected at the core. Upon examining the infrared morphology, Anderson et al. (2011) found that more than half of the HRDS H II regions exhibited bubble morphology, which aligns closely with our findings.
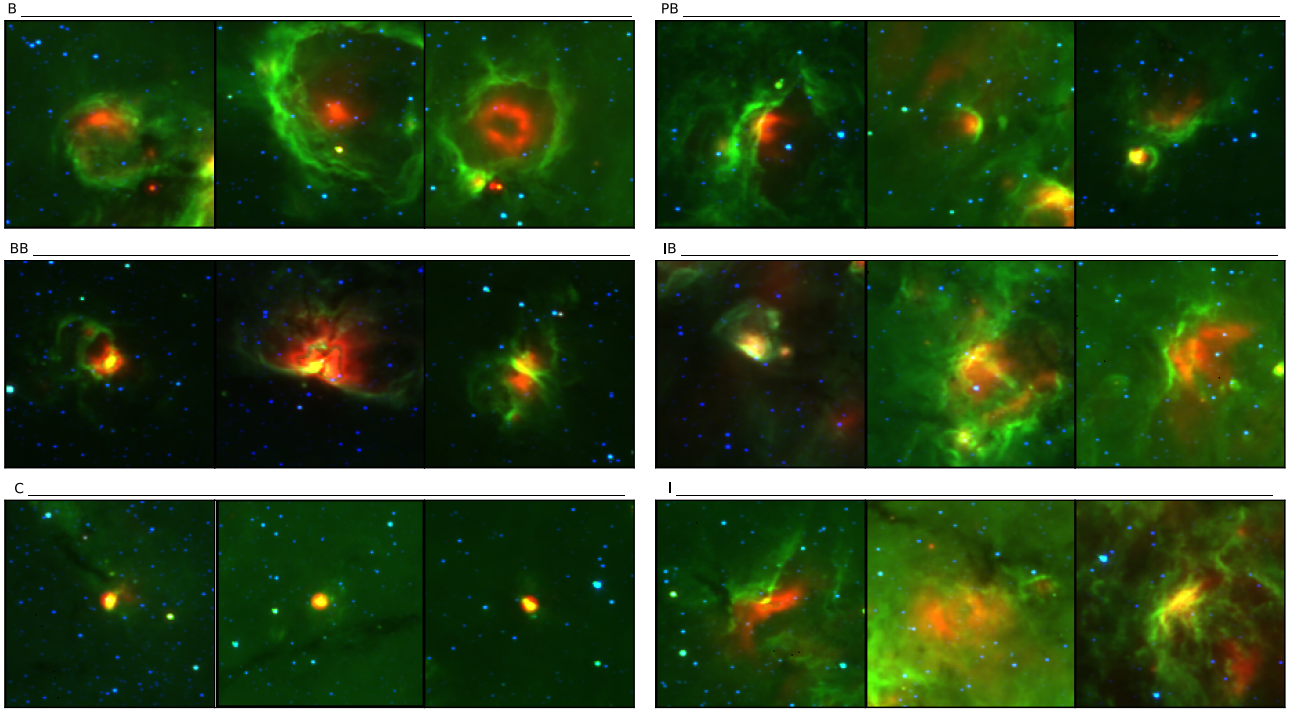
Fig. 11. Example of GLOSTAR H II region morphological classifications. In each panel, a three-color image is generated using *Spitzer* infrared data: MIPSGAL 24 μm data represented in red, GLIMPSE 8.0 μm data in green, and GLIMPSE 3.6 μm data in blue.

Table 3. Classification of the MIR morphology of H II regions.

	B	BB	PB	IB	C	I	ND
Galactic center	2	0	2	2	9	11	2
Cygnus X	1	0	2	2	1	6	1
Galactic disk [(*)]	30	13	31	32	32	59	6
Total	33	13	35	36	42	76	9

Notes. We categorized the 8 μm emissions from *Spitzer* GLIMPSE as follows: B – Bubble, featuring 8 μm emission surrounding 24 μm; BB – Bipolar Bubble, consisting of two connected bubbles with a region of strong infrared; PB – Partial Bubble, similar to a bubble but incomplete; IB – Irregular Bubble, lacking a well-defined structure; C – Compact, exhibiting compact 8 μm emission; I – Irregular Structure, displaying complex morphology that cannot be easily classified; and ND – Not Detected, indicating either a lack of 8 μm emission or very weak emission. [(*)]Here, by Galactic disk, we mean the region of the Galaxy within $2° \leq \ell \leq 60°$, $|b| \leq 1°$.

Through visual examination of images from the GLIMPSE survey, Churchwell et al. (2006, 2007) compiled a catalog of 591 Galactic bubbles. However, we only identified RRLs originating from ionized gas in 15 of the 250 GLIMPSE bubble sources in the GLOSTAR survey region. This limited correlation could be attributed to the limited sensitivity of our interferometry observations for large structures.

The cumulative distribution function (CDF) is a statistical tool that illustrates how data points are distributed across a range of values and facilitates straightforward comparisons between diverse datasets or groups of data. Fig. 12 presents the CDFs of GLOSTAR survey H II regions, divided into bubble and non-bubble categories. The non-bubble category includes compact and irregular H II regions. To ensure the validity of our analysis, we excluded H II regions located in the Galactic center region,

as the complicated emission structures that are prevalent there might affect the morphology classification compared to the rest of the Galactic plane. Various H II region properties, such as RRL width, electron temperature, electron density, EM, Lyman continuum photon rate, and ionized gas mass, were examined. A comparison was conducted between a total of 111 bubble H II region and 104 non-bubble H II regions. To assess the statistical significance of differences between the two groups, Anderson-Darling (AD) tests were conducted on all CDFs. The findings are depicted in Fig. 12. Interestingly, we observed no statistically significant differences in most of the H II region properties between the two groups, except for RRL width and electron density, where the p-value was < 0.05 (significance level of 2σ). The mean RRL width of non-bubble H II regions is 28.4 km s^{-1}, which is slightly wider than the average line-width of bubble H II regions, which is 25.7 km s^{-1}. This contrasts with Anderson et al. (2011), who found that the average RRL width of bubble sources was identical to the entire HRDS sample. However, the significant level of difference in RRL width is only up to 2σ, which is not conclusive. According to the ring scenario proposed by Beaumont & Williams (2010), which suggests that "bubble" sources are physically two-dimensional rings, we would expect RRL widths for bubbles to be larger than those of the rest of the H II region sample. This is because both red-shifted and blue-shifted ionized gas from the bipolar flow contribute to the bubble line width (Anderson et al. 2011). However, our findings show the opposite, suggesting that bubbles are three-dimensional structures.

Churchwell et al. (2006, 2007) and Simpson et al. (2012) have demonstrated that bubbles are widespread in IR images of the Galactic plane and compiled a large population of Galactic IR bubbles. These bubble structures in the ISM can arise from various astronomical phenomena, not limited to young, massive stars. Evolved objects such as supernova remnants, PNe, Wolf-Rayet stars, and (post)-AGB stars can also form bubbles.
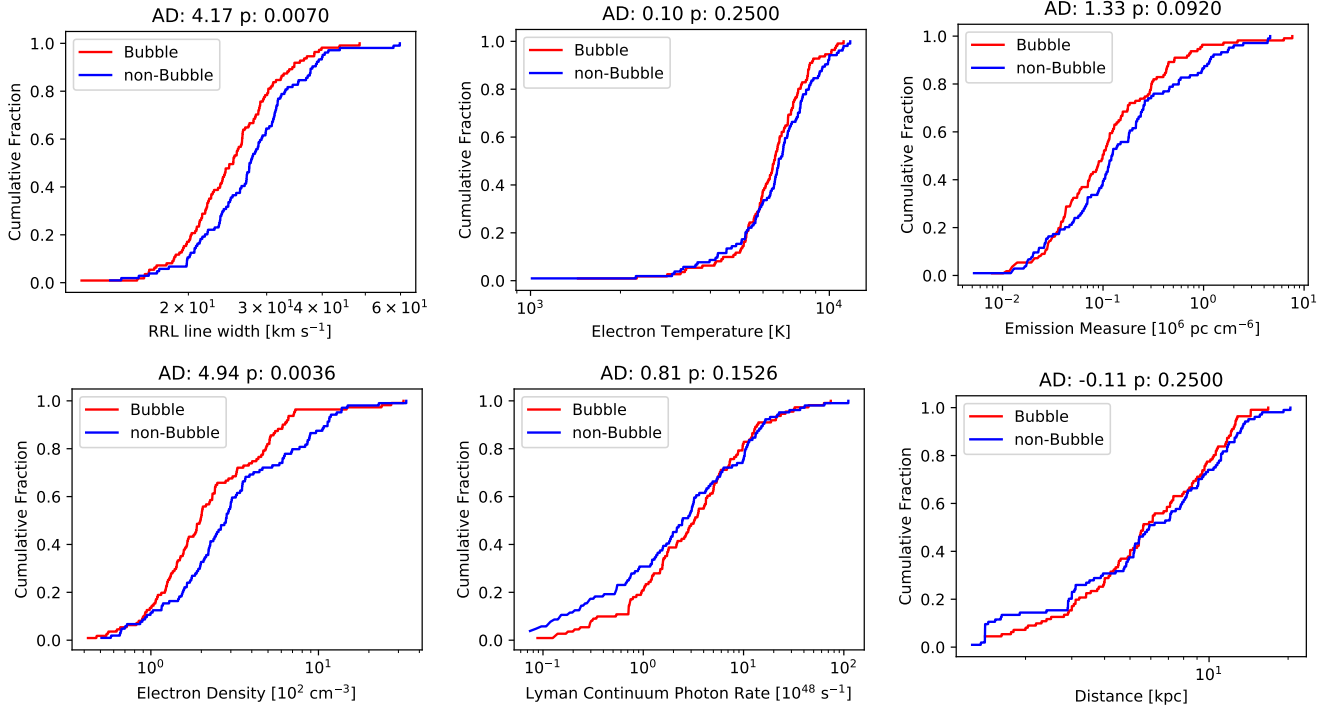
Fig. 12. CDFs for various properties of GLOSTAR H II regions. We compare the sample of the GLOSTAR H II regions with Bubble morphology (in red) to the sample of GLOSTAR H II regions non-bubble morphology (in blue). The results of the Anderson-Darling (AD) tests are presented above each plot.

Deharveng et al. (2010) proposed that at least 86% of the Galactic bubbles are associated with H II regions. Additionally, Anderson et al. (2011) and this work showed that approximately 50% of the H II regions exhibit bubble morphology at 8.0 μm. These findings suggest that almost all Galactic bubbles are H II regions, but not all H II regions show a bubble-like structure. Studies conducted with a lower angular resolution than ours, indeed confirm a considerably larger population of H II regions in the Galactic plane, as is discussed in Anderson et al. (2014).

5.2. Association with dust emission

Ultracompact and compact H II regions usually have associated dust emission from molecular clouds in which their ionizing massive stars have been born. Even later-type O-type stars and early B-type stars are often associated molecular clouds whose dust is heated by the radiation from them (Churchwell 2002). Thompson et al. (2006) surveyed the environments of 105 IRAS point sources at 850 and 450 μm for a comprehensive study on the association of sub-millimeter dust emission with UC H II regions. They reported three distinct types of objects: UC cm-wave sources that are not associated with any submillimeter emission ("submillimeter quiet objects"), submillimeter clumps that are associated with UC cm-wave sources ("radio-loud clumps"); and submillimeter clumps that are not associated with any known UC cm-wave sources ("radio-quiet clumps"). Inspired by this, we studied the dust association of the detected 202 H II regions within $3° \leq \ell \leq 60°$, and $|b| \leq 1°$ and categorized these objects into "submillimeter quiet H II regions" or "submillimeter loud H II region".

We examined dust clumps within the above range from the ATLASGAL compact source catalog (CSC; Urquhart et al. 2014). For ATLASGAL CSC objects, Urquhart et al. (2018, 2022) determined clump mass, dust temperature, bolometric

luminosity and V_{LSR} velocity. We performed a crossmatch with ATLASGAL sources using a angular separation threshold of 12″, which is three times the uncertainty in ATLASGAL position and half of GLOSTAR RRL image beam size. We found 97 associations within 12″ (48%). Out of these 97 associated dust clumps, 68 are classified as H II regions, whereas 22, 4, and 3 sources are classified as photo-dissociation regions (PDRs), Ambiguous, or Complicated by Urquhart et al. (2022). We also observed that the average angular offset for the H II regions association is 6.2″ which is slightly smaller than the angular offset for the other source types which is 8.0″. In the following, we focus our attention on these 68 H II regions labeled as submillimeter loud H II regions and further explore their association with the corresponding dust clumps.

In Fig. 13, the LSR velocities of ATLASGAL dust clumps are compared with the RRL peak velocities measured in GLOSTAR. The velocities of the ATLASGAL sources were determined by observations of spectral lines from multiple molecular line surveys toward them (see Sect. 2.1 of Urquhart et al. 2018, for more details). A linear fit was performed, resulting in a slope of 0.96 ± 0.02 and a y-intercept of 3.5 ± 1.3 km s^{-1}, respectively. The Spearman's correlation coefficient of 0.98 indicates a positive correlation. A Gaussian function was used to fit the distribution of velocity offsets, which yielded a mean offset of -0.62 ± 0.12 km s^{-1} and a standard deviation of 10.5 ± 0.3 km s^{-1}. This indicates a small velocity offset between the molecular gas and the ionized gas associated with H II regions. The results are in excellent agreement with the findings of Anderson et al. (2009), for their study of molecular properties of the Galactic H II regions. This study revealed a standard deviation of 8.5 km s^{-1} and a mean of 0.2 km s^{-1} for the distribution of the LSR velocity difference between the RRL and ^{13}CO velocities. These values are also similar to those found in the WISE catalog of Galactic H II regions by Anderson et al. (2014). This
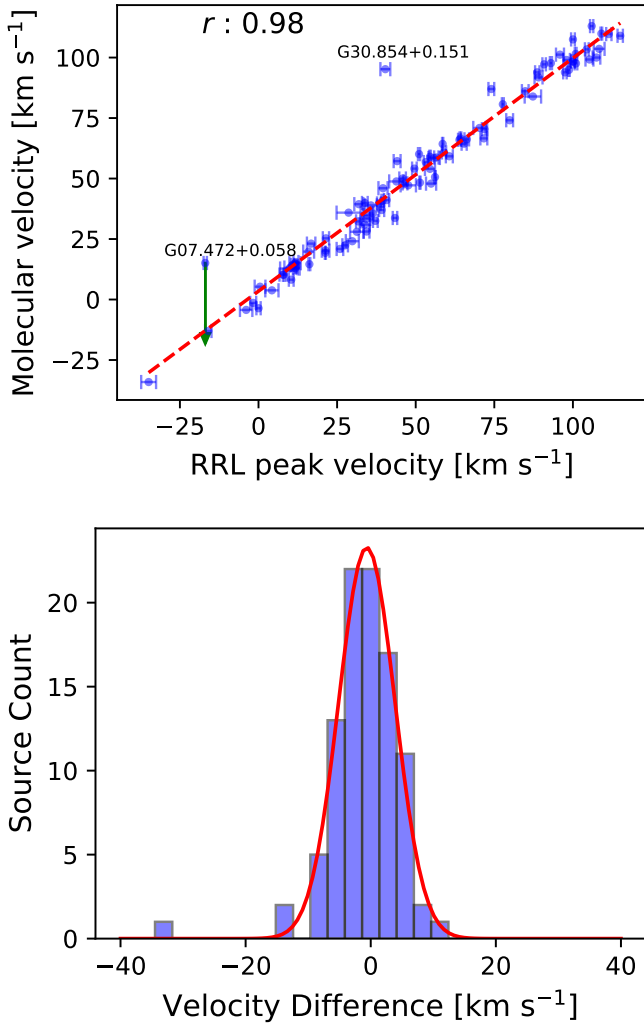
Fig. 13. Comparison between the RRL peak velocity and ATLAS-GAL dust clump velocity. Top: the RRL peak velocity is plotted against the ATLASGAL clump velocity. The red line shows a linear fit, with a Spearman's rank coefficient of $r = 0.98$ and p-value $\ll 0.0013$. The linear fit produces a slope of 0.96 ± 0.02 and a y-intercept of 3.5 ± 1.3 km s^{-1}. The green arrow shows the direction of the corrected velocity of G007.472+0.058. Bottom: the distribution of velocity offsets between the RRL peak velocities and the molecular line velocities from ATLASGAL is shown. Fitting the distribution with a Gaussian function yields a mean offset of -0.62 ± 0.12 km s^{-1} and a standard deviation of 10.5 ± 0.3 km s^{-1}.

shows that the velocities of ionized gas in H II regions are in good agreement with those of the molecular gas from which the massive stars formed.

There are two sources with velocity offsets greater than 3σ: G007.472+0.058 (AGAL007.471+00.059) and G030.854+0.151 (AGAL030.854+00.149). For the latter, Urquhart et al. (2018) assigned the molecular LSR velocity based on NH$_3$ line observations by Wienen et al. (2012). Wienen et al. (2012) detected strong emission in the NH$_3$ (1,1), (2,2) and (3,3) transitions, toward this source. These transitions revealed the source velocity to be 95.2 km s^{-1}, resulting in a velocity offset of -54.86 km s^{-1}. Anderson et al. (2011) reported multiple RRL velocity components for G030.854+0.151 (HRDS name: G030.852+0.149), with the brightest component at 39.6 km s^{-1}, while the other two weaker components are at 88.7 and 114.5 km s^{-1}. Additionally, this source is in the direction of W43, which is located close

to the near end of the Galactic bar and the inner Scutum arm, a region of intricate gas dynamics (Nguyen Luong et al. 2011; Luisi et al. 2020). Anderson et al. (2015) suggested that the additional velocity components are associated with the diffuse Warm Ionized Medium (WIM). However, it is unlikely that GLOSTAR D-configuration observation would be able to detect the diffuse gas of the WIM. Hence, in this case the large velocity offset could be attributed to the fact that the velocities of our RRLs and the NH$_3$ transitions observed by Wienen et al. (2012) probe different regions along the line of sight. In the case of G007.472+0.058 (AGAL007.471+00.059), the source exhibits two peaks of ^{13}CO emission at 15.07 km s^{-1} and -14.44 km s^{-1}, and a single peak of C^{18}O emission at 15.10 km s^{-1} (Urquhart et al. 2018). However, Urquhart et al. (2018) assigned the velocity to this source based on the single peak of C^{18}O. Rathborne et al. (2016) showed that the molecular velocity of AGAL007.471+00.059 is -13.91 km s^{-1}, based on the intensity weighted velocities of HCO$^+$, HCN, and N$_2$H$^+$ lines. Taking the latter, the LSR velocity difference between the molecular and ionized gas emission of AGAL007.471+00.059 is 3.03 km s^{-1} ($< 3\sigma$), which is consistent with the velocity offset distribution of the sample.

In Fig. 14, we show the CDFs for GLOSTAR H II region properties, including electron temperature, electron density, EM, Lyman continuum photon rate, ionized gas mass and distance for submillimeter loud and submillimeter quiet H II regions. A total of 68 submillimeter loud H II regions with associated dust clumps are compared to 134 submillimeter quiet H II regions without any dust association. Inspection of the electron density and EM (top middle and right panel of Fig. 14), revealed a significant difference between the submillimeter loud and submillimeter quiet H II regions (AD test return a p-value $\ll$ 0.0013). Fig. 14 shows that the n_e and EM are higher for submillimeter loud H II region as they are likely to be smaller and denser. Turning our attention to the Lyman photon rate (bottom left of Fig. 14), we see a significant difference at the 3σ level (p-value < 0.0013) between submillimeter loud and submillimeter quiet H II regions. Additionally, we also notice that the Lyman continuum flux for the submillimeter loud H II region is slightly higher compared to the submillimeter quiet H II region. It is not very clear why they are hotter and have more Lyman continuum flux. It is possible that as the H II regions evolve they become more extended, resulting in underestimation of Lyman continuum flux due to interferometric filtering of diffuse emission. Examining the electron temperature, we notice that the distribution becomes indistinguishable at higher values, which is not the case for lower electron temperatures. The AD test reveals a significant difference at the 3σ level (p-value $\sim$0.0013) between submillimeter loud and submillimeter quiet H II regions. In addition to electron density and EM, we also observe that the electron temperature of the submillimeter loud is higher than that of submillimeter quiet H II regions. This is not unexpected as the higher value of n_e is expected to produce higher value of T_e (as mentioned in Sect. 4.3.3). Examining ionized gas mass and distance, we observe that the distributions of submillimeter loud and submillimeter quiet H II regions are indistinguishable from each other.

5.3. Association with 6.7 GHz methanol masers

Class II methanol maser emission in the 6.7 GHz line was first discovered by Menten (1991), and since then, these masers have proven to be valuable tools for investigating high-mass star-forming regions. The 6.7 GHz methanol masers are exclusive
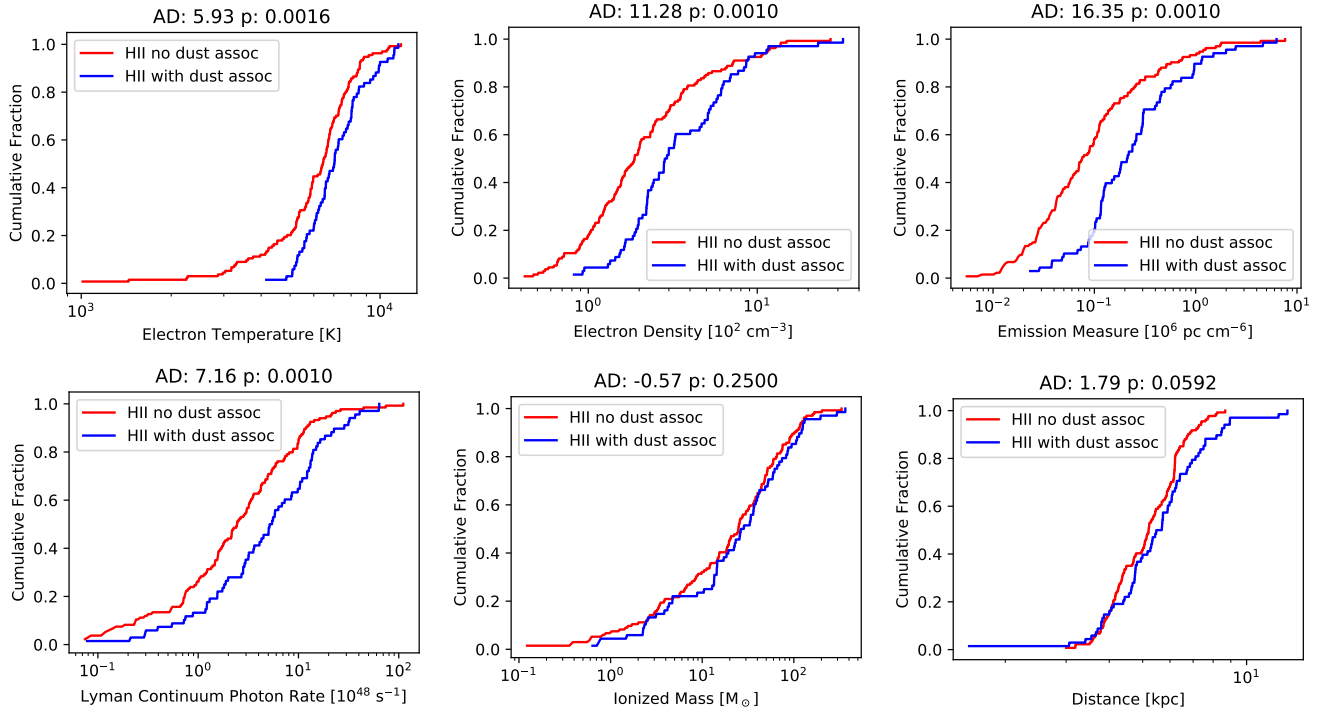
Fig. 14. Comparison between the properties of GLOSTAR H II regions that are associated with ATLASGAL dust clumps (in red) and those that are not linked to ATLASGAL clumps (in blue). CDFs are presented for various properties of GLOSTAR H II regions. The results of the Anderson-Darling (AD) tests, indicated above each plot, provide insights into the statistical significance of the observed differences.

tracers of the early evolutionary stages of high-mass stars (e.g., Urquhart et al. 2015; Paulson & Pandian 2020). Yang et al. (2021) suggests that younger H II regions are more likely to be associated with masers as the detection rate of maser emission decreases as H II regions evolve from HC H II regions to UC H II regions. This is supported by the detection of methanol masers toward Galactic H II regions, which seem to be closely correlated with compact H II regions (Walsh et al. 1998; Ouyang et al. 2019; Chen et al. 2020b). However, the studies conducted by Hu et al. (2016) and Nguyen et al. (2022) did not reveal any apparent correlation between the flux density from methanol masers and radio continuum sources. This indicates that methanol maser and radio continuum sources exhibit independent luminosity behaviors.

The GLOSTAR survey (Brunthaler et al. 2021) observed RRLs and Class II 6.7 GHz methanol (CH₃OH) masers simultaneously, allowing accurate results of cross matching of their positions. Ortiz-León et al. (2021) and Nguyen et al. (2022) compiled a catalog of 6.7 GHz methanol masers within the region covered by the GLOSTAR survey in the Galactic plane, using the VLA D-configuration data. We conducted an investigation to identify potential correlations between RRLs and 6.7 GHz methanol masers detected in the GLOSTAR VLA D-configuration data (Nguyen et al. 2022) within the Galactic zone of $2° \leq \ell \leq 60°$, $|b| \leq 1°$. We find a total of 30 ($\sim 15\%$) cross matches within a radius of 12″, which is half of the size of the GLOSTAR RRL beam. The mean ± standard deviation of the separation between methanol maser position and continuum peak is $6.0 \pm 2.6″$. This number goes down to 17 ($\sim 8\%$) sources, when we use an angular distance threshold of 6″, which was used by Nguyen et al. (2022) to study the association of methanol masers with GLOSTAR D-configuration continuum sources. Hu et al. (2016) propose two criteria for determining the association between maser and continuum sources based on their projected

spatial distance. Firstly, the projected spatial distance between peak positions of the maser and continuum sources should be smaller than 1 pc, and secondly, it should be less than the major axis of the continuum source. In all 30 cases, the projected spatial offset is less than 1 pc, with a mean separation of 0.2 pc. Also, for all cases the projected spatial offsets are smaller than the effective diameters of the host H II regions. Using the catalog of methanol masers compiled by Nguyen et al. (2022) and Ortiz-León et al. (2021), we find only 13% (30/202) of the H II regions have associated methanol maser emission within a radius of 12″. For comparison, Anderson et al. (2011) found 10% of the HRDS H II regions to have associated methanol masers. Walsh et al. (1998) observed that 38% of the sources in their UC H II region sample have methanol maser emission. In the study by Ouyang et al. (2019), out of 98 radio continuum sources, 23 sources were detected with both RRL and methanol maser emission. Chen et al. (2020b) reported that 20% of the sources with RRL detection were found to be associated with methanol masers. These comparisons suggest that most of the H II regions in our sample might not be as young as UC/HC H II regions.

Fig. 15 shows the correlation of RRL peak velocity and median methanol maser velocity. All the associated RRL and methanol masers source exhibit similar velocities with a Spearman's rank coefficient of $r = 0.98$ and p-value $\ll 0.0013$, which intrinsically represents the systemic motion of the sources. Fig. 15 presents the distribution of the velocity difference. Fitting the distribution with a Gaussian function yields a mean of 0.5 ± 0.3 km s^{-1} and a standard deviation of 4.0 ± 0.34 km s^{-1}. These results show a strong agreement between RRL and methanol maser velocities and indicating that they are associated with the same molecular cloud.

The mean values of continuum flux densities and RRL integrated intensities for H II regions associated with methanol masers are slightly lower (1.8 Jy and 6.7 Jy km s^{-1}, respectively)
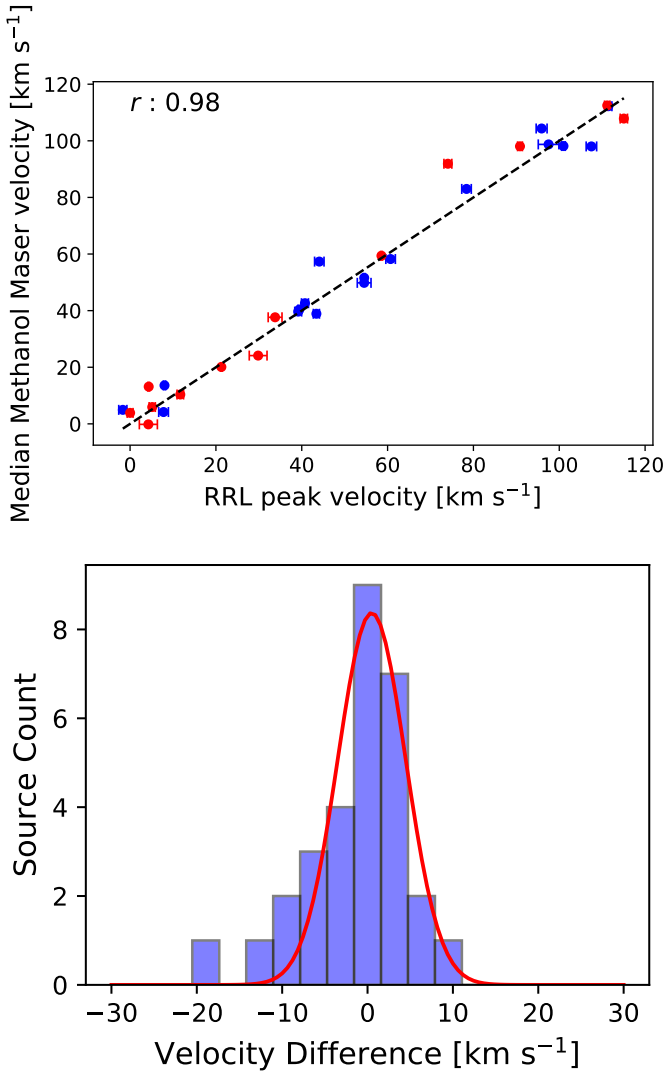
Fig. 15. Comparison between the RRL peak velocity and median methanol maser velocity. Top: the RRL peak velocity is plotted against the median methanol maser velocity. Sources with a positional offset between the H II region and methanol maser of less than 6″ are depicted using blue circles, while sources with a positional offset greater than 6″ but less than 12″ are represented by red circles. The dashed black line represents the line of equality, x=y, with a Spearman's rank coefficient of $r = 0.98$ and p-value $\ll 0.0013$. Bottom: the distribution of velocity offsets between the RRL peak velocities and median methanol maser velocity is shown. Fitting the distribution with Gaussian yield a mean of 0.5 ± 0.3 km s^{-1} and standard deviation of 4.0 ± 0.34 km s^{-1}.

compared to those without maser emissions (2.4 Jy and 9.1 Jy km s^{-1}, respectively). This finding supports the notion that methanol masers are linked to younger H II regions (Yang et al. 2019, 2021; Walsh et al. 1998). However, it is essential to note significant differences in the sample size, which may influence the interpretation of these results. In Fig. 16, we present the maser integrated flux density plotted against both the continuum flux density and the RRL integrated intensity. The Spearman's rank coefficient for the correlation between maser integrated flux density and continuum flux density is –0.196, with a p-value of 0.64, indicating no significant correlation between these properties. This is consistent with the conclusions drawn by Hu et al. (2016) and Nguyen et al. (2022). However, Ouyang et al. (2019), reported a strong positive correlation of luminosity

between 6.7 GHz methanol maser and RRLs. In this regard, it is worth noting that their angular resolution (∼3′) was significantly poorer compared to that of GLOSTAR. Similarly, the correlation between maser integrated flux density and RRL integrated intensity yields a Spearman's rank coefficient of –0.203, with a p-value of 0.43, also suggesting no significant correlation between these two variables. The methanol maser line width as a function of the RRL width is also shown in Fig. 16 with the Spearman's rank coefficient $r = -0.035$, and a p-value of 0.43, suggesting no relation. These findings indicate that the mechanisms responsible for powering masers and exciting RRLs are not related to each other.

In Fig. 17, we show the CDFs of H II regions categorized by the presence or absence of detected methanol masers to compare various H II region properties, such as RRL amplitude, RRL width, T_e, EM, n_e, and N_{Lyc}, and distance. The sample consists of 32 H II regions associated with methanol masers and 212 H II regions without methanol masers. Nguyen et al. (2022) compared the flux density of continuum sources that have 6.7 GHz methanol maser association and those without. They found that the radio sources with the methanol maser are significantly brighter than the general population of radio sources. From this, we can expect that the RRL amplitude of H II regions associated with methanol maser to be brighter than those without. In contrast, looking at the CDFs of RRL amplitude (top left panel of Fig. 17) and RRL width (top middle panel of Fig. 17), we did not notice a significant difference in the distribution. Similarly, for T_e, N_{Lyc}, and distance, we see that the distributions are indistinguishable from each other. The electron density and EM of H II regions is statistically different property at the 3σ level (AD test results in p-value $\ll 0.0013$). We see that electron density and EM of the H II regions with the methanol maser are significantly higher than the H II regions without methanol masers. This suggests that methanol masers are associated with denser H II regions, which is not unexpected since methanol masers typically appear in the early phases of star formation, characterized by higher densities, as reported by Yang et al. (2021). Furthermore, we see that the mean values of H II region properties such as electron temperature, and Lyman photon rate of H II regions associated with methanol masers are slightly higher compared to those without maser emission.

We give the average value of physical properties of H II regions associated with the dust emission, 6.7 GHz methanol maser and bubble morphology in MIR in Table 4. The average values of n_e, EM and N_{Lyc} are higher in the early stage of evolution of H II regions (methanol masers and submillimeter loud) compared to the evolved stage (submillimeter quiet), which is consistent with the standard picture. We did not notice prominent trend in the average value of T_e and ionized gas mass. We show a Venn diagram of the correlation between the association of H II regions with the dust emission, 6.7 GHz methanol masers, and bubble morphology over a common Galactic region of $2° \leq \ell \leq 60°$, $|b| \leq 1°$ in Fig. 18. There is a strong correlation between the H II regions associated with the dust emission and 6.7 GHz methanol masers.

5.4. Galactic electron temperature gradient

Churchwell & Walmsley (1975) were the first to investigate the correlation between the electron temperatures of H II regions and their distance from the center of the Galaxy (R_{Gal}). Subsequent studies, such as Churchwell et al. (1978), Shaver et al. (1983), Wink et al. (1983), and Quireza et al. (2006), confirmed this gradient in the electron temperature across the Galaxy, namely that
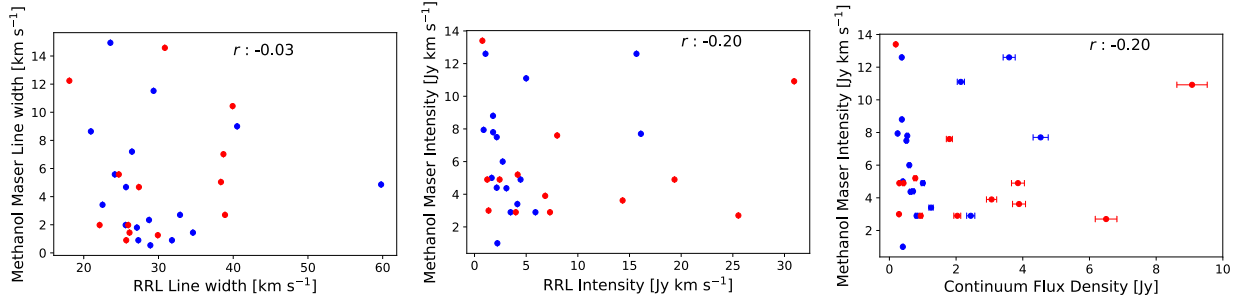
Fig. 16. Left: RRL width plotted as a function of the methanol maser line width. RRL integrated intensity (middle) and continuum flux density (right) plotted as a function of maser integrated intensity. Blue and red circle corresponds to a separation of less and more than 6″ respectively. Sources with a positional offset between the H II region and methanol maser of less than 6″ are depicted using filled black circles, while sources with a positional offset greater than 6″ but less than 12″ are represented by black circles. There appears to be no evident correlation between the strengths of the continuum or RRL and the maser. Additionally, no correlation is found between the line width of the RRL and the maser signals.
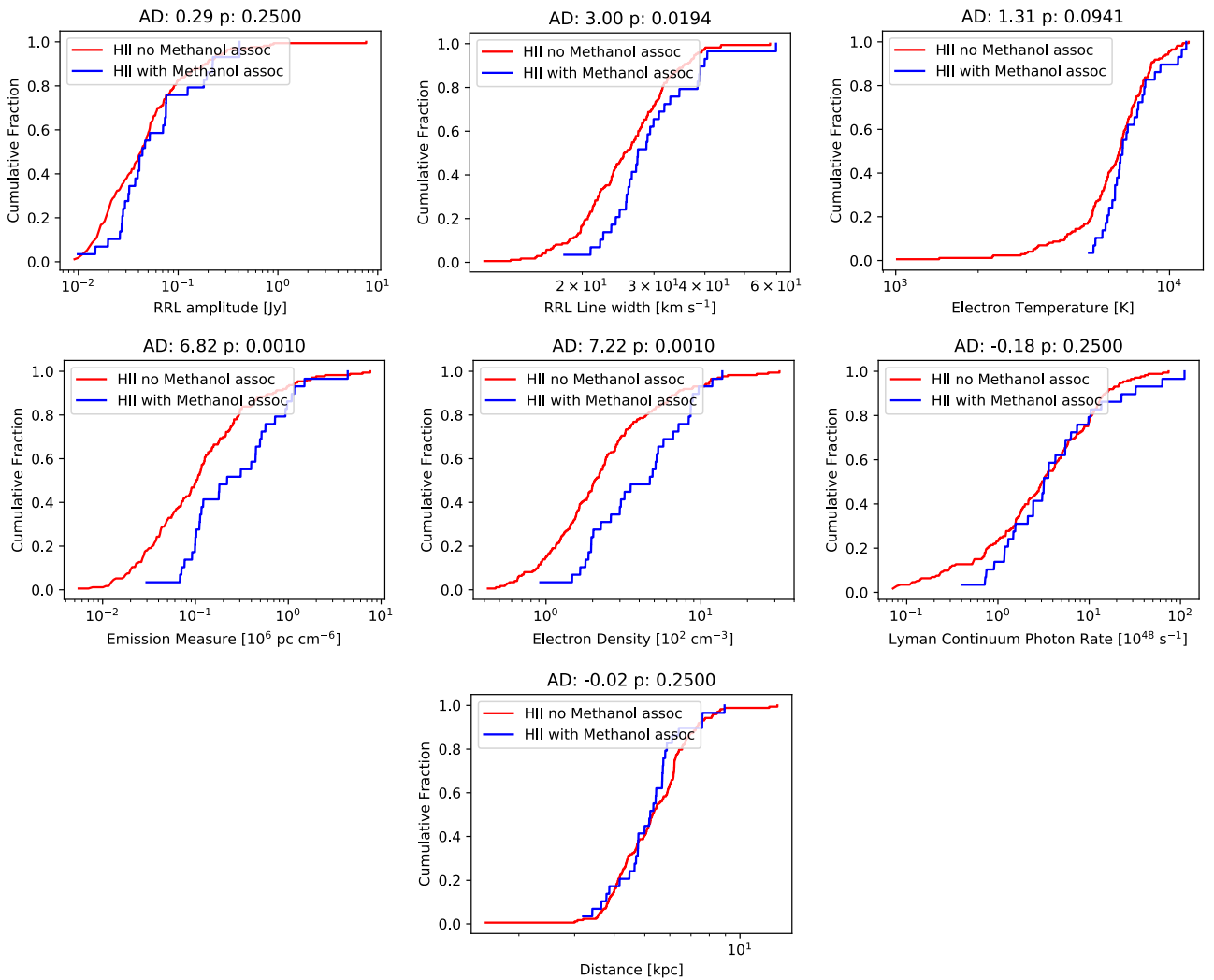
Fig. 17. CDFs for various properties of GLOSTAR H II regions. We compare the sample of the GLOSTAR H II regions associated with methanol masers (in blue) to the sample of GLOSTAR H II regions not associated with methanol masers (in red). The results of the Anderson-Darling (AD) test are presented above each plot.

T_e is lower in the Galactic center and increases with R_{Gal}. However, there are still uncertainties regarding the exact magnitude of this gradient and the possibility of its variations with Galactic azimuth.

In this study, we determine the electron temperatures of H II regions for a large sample of H II regions located in the first quadrant of the Galactic disk. Our H II region sample consists of 244 H II regions out of which 29 are located close to the Galactic center region ($-2° \leq \ell \leq 2°$, $|b| \leq 1°$). Due to lack of reliable distance estimates for these H II regions (see Sect. 4.2), we focused on 215 sources to investigate the gradient across the Galactic plane with R_{Gal} ranging from 1.5 to 9.1 kpc. Within

Table 4. Averaged physical properties of H II regions associated with the dust emission, 6.7 GHz methanol masers, and bubble morphology over a common Galactic region of $2° \leq \ell \leq 60°$, $|b| \leq 1°$.

H II region association	T_e (10^3 K)	EM (10^5 pc cm^{-6})	n_e (10^2 cm^{-3})	N_{Lyc} (10^{48} s^{-1})	Mass$_{H II}$ ($M_\odot$)
Methanol maser	7.3 ± 0.7	5.2 ± 0.4	5.2 ± 0.2	10.0 ± 0.4	28.5 ± 1.1
Submillimeter loud	7.3 ± 0.8	5.1 ± 0.4	4.9 ± 0.2	7.9 ± 0.3	33.4 ± 2.0
Submillimeter quiet	6.2 ± 0.9	2.8 ± 0.2	3.2 ± 0.2	5.5 ± 0.3	31.1 ± 2.2
Bubble	6.5 ± 0.9	3.0 ± 0.2	3.1 ± 0.1	6.7 ± 0.3	38.0 ± 2.3
Average	6.6 ± 0.9	3.6 ± 0.3	3.8 ± 0.2	6.3 ± 0.3	32.0 ± 2.1
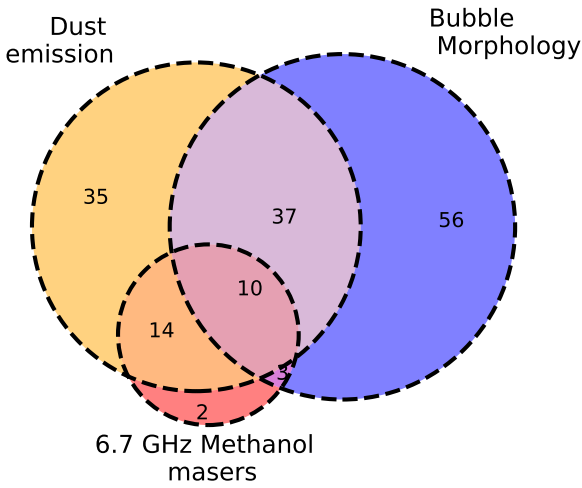
Fig. 18. Venn diagram showing the correlation between the association of H II regions with the dust emission, 6.7 GHz methanol masers, and bubble morphology over a common Galactic region of $2° \leq \ell \leq 60°$, $|b| \leq 1°$.

this subset, two H II regions stand out as anomalies, deviating from the overall trend in T_e, exhibiting significantly lower temperatures: G025.479–0.174 (with a temperature of 1010 K and located at a distance of 4.95 kpc) and G030.870–0.099 (with a temperature of 1441 K and located at a distance of 4.85 kpc).

To analyze the gradient, we derived the Galactic electron temperature gradient for two different cases. The first subset consisted of all 213 sources from this work, while the second subset included 496 sources out of these 213, 116, and 167 H II regions from this work, Quireza et al. (2006) and Wenger et al. (2019), respectively. We performed the Bayesian linear regression with Markov chain Monte Carlo (MCMC) sampling separately for both cases. We utilized *scipy.stats.linregress*[9] to model the temperature gradient as a linear function, represented by $T_e = a_1 + a_2 R_{Gal}$ K. To implement the MCMC, we used the python package *emcee*[10] (Foreman-Mackey et al. 2013), which allowed us to estimate the posterior probability distribution of the model parameters (slope and intercept). To visualize the results, we generated a corner plot using the python package *corner.py*[11] (Foreman-Mackey 2016). In Fig. 19, we present the fit results along with the corner plot. Each histogram in the corner plot represents the posterior distribution of a parameter, with the width of the histogram indicating the uncertainty

associated with that parameter. Additionally, the scatter plot in the corner plot displays the joint distribution between two parameters. We present the gradient fit obtained from the first sample, which comprised 213 data points with R_{Gal} spanning from 1.6 to 13.1 kpc. The gradient fit for this sample was determined to be $T_e = (372 \pm 28) R_{Gal} + (4248 \pm 161)$ K. The gradient fit for the second sample was determined to be $T_e = (293 \pm 2) R_{Gal} + (5278 \pm 15)$ K within R_{Gal} range of 0.1 to 20.0 kpc. The shallower slope for the latter case might be due to the exclusion of the Galactic center H II regions and a much wider range of R_{Gal}.

Upon comparing our study with previous research, we found that our derived electron temperature gradient aligns well with the reported values. Quireza et al. (2006) obtained a gradient of 287 ± 46 K kpc^{-1} using 76 Galactic H II regions within the range $R_{Gal} = 0.0$–17.0 kpc. After excluding the Galactic center sources, they found the slope to be 340 ± 45 K kpc^{-1}, using the 73 Galactic H II regions located in the range, $R_{Gal} = 2.0$–17.0 kpc. Wenger et al. (2019) used Monte Carlo analysis to derive the most likely Galactic radial electron temperature gradient as 359^{+22}_{-18} K kpc^{-1}. Balser et al. (2011) reported a gradient of 299 ± 33 K kpc^{-1} using 133 sources within the range $R_{Gal} = 0.1$–21.9 kpc. These electron temperature gradients vary around 300 K kpc^{-1}. However, a few previous studies reported very steep gradients, such as 433 ± 40 K kpc^{-1} by Shaver et al. (1983) with a sample of $N=67$ Galactic H II regions in the range $R_{Gal} = 3.5$–13.7 kpc, 440 ± 50 K kpc^{-1} ($N=23$, $R_{Gal} = 3.6$–12.6 kpc) by Garay & Rodriguez (1983), and 372 ± 38 K kpc^{-1} ($N=6$, $R_{Gal} = 6.6$–14.8 kpc) by Deharveng et al. (2000).

We observe a scatter in the H II region electron temperature at a given Galactocentric radius. One explanation could be the presence of systematic uncertainties in determining the electron temperature. However, in our case, we do not anticipate any systematic errors in estimating the electron temperature. This is because the VLA enables simultaneous measurement of both radio-continuum and RRL emissions, and the RRL-to-continuum flux ratio enables us to mitigate any systematic calibration or weather-related concerns. Another major factor that might contribute to the fluctuation in the T_e gradient is the variation in metallicity as reported by previous studies such as Quireza et al. (2006), Balser et al. (2011), Wenger et al. (2019). The electron temperature is an outcome of heating by radiation from the massive stars and cooling by fine structure lines. With change in metallicity, the cooling function will change significantly giving a different equilibrium temperature (Shaver et al. 1983).
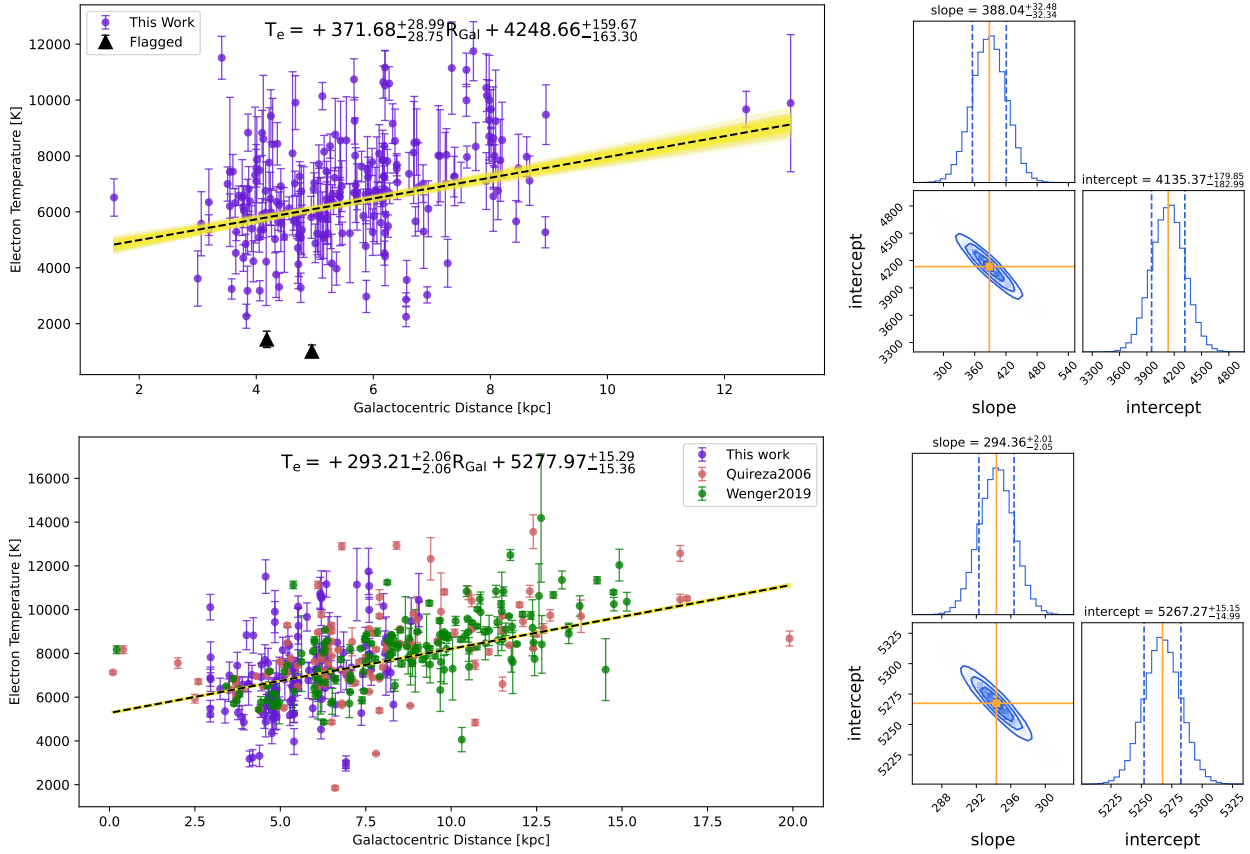
6. Summary

In this study, we conducted an unbiased survey of Galactic H II regions in the Galactic plane ($-2° \leq \ell \leq 60°$ and $|b| \leq 1°$, and

---

[9] https://docs.scipy.org/doc/scipy/reference/generated/scipy.stats.linregress.html
[10] https://emcee.readthedocs.io/en/stable/
[11] https://corner.readthedocs.io/en/latest/

Fig. 19. Most likely electron temperature gradient determined using the Bayesian linear regression with the MCMC sampling for different samples. The left panel shows the data and the most likely linear model in the dashed black line. The error bars are 1σ uncertainty in the derived electron temperature. The shaded yellow region represents the range of fits from 10 000 MCMC iterations. The black triangles represent the outlier data points which are flagged before the fitting, while the filled purple circles represent the data used for fitting. The right panel shows the corresponding corner plot displaying the one-dimensional (1D) histogram of the posterior distribution for each parameter (slope and y-intercept). The histograms represent the probability density functions (PDFs) of the Monte Carlo fit parameters, while the blue curves represent the scatter plot of the joint distribution between the two parameters. The solid orange lines indicate the peaks of the PDFs, representing the most likely fit parameters, and the dotted blue lines correspond to the 1σ confidence intervals. Top panel: Case 1: Consists of all 213 sources in our catalog excluding the Galactic center H II due to lack of reliable distance estimate. Bottom panel: Case 2: consists of 496 sources located within R_{Gal} range of 0.1–20.0 kpc from Quireza et al. (2006), Wenger et al. (2019), and our catalog. The electron temperature gradient for each sample is given in the plots.

$76° \leq \ell \leq 83°$ and $-1° \leq b \leq 2°$) that are covered by GLOSTAR. By utilizing the RRL data obtained with the VLA in D-configuration with an angular resolution of $25''$ and a typical 1σ noise level of ~3.0 mJy beam^{-1} at a velocity resolution of ~5 km s^{-1}, we compiled a catalog of 244 Galactic H II regions, along with their physical properties. The main findings are as follows:

– The mean value of the RRL width is ~28 km s^{-1}, which is > 425 km s^{-1}. Compared to previous H II region surveys, our samples exhibit comparable, if slightly broader, RRL widths. We identified 23 sources with broad line widths > 35 km s^{-1}, of which 15 are associated with candidate HC H II regions;
– 48% of the GLOSTAR H II regions show a bubble-like morphology in GLIMPSE 8.0 µm images. AD tests reveal no statistically significant differences in most of the H II region properties between the bubble and non-bubble H II regions, except for a wider RRL width and a higher electron density in non-bubble HII regions that shows a significant difference at only 2σ;
– Comparing the H II regions with the ATLASGAL Compact Source Catalog (CSC), we find that 48% of them are associated with the ATLASGAL dust clumps, which we term submillimeter loud H II regions. The comparison of

velocities derived from RRLs and molecular lines reveals an excellent agreement between the ionized gas and molecular gas;
– AD tests on the CDFs of submillimeter loud H II regions and submillimeter quiet H II regions reveal that, apart from electron density, EM, and electron temperature, no other ionized gas properties change as an H II region evolves from a dust-associated H II region to a dust-quiet one;
– Upon crossmatching with the GLOSTAR methanol maser catalog, we found that only 15% of H II regions in our sample were associated with methanol maser emissions. Based on the AD test, we found that H II regions with methanol masers show a significantly higher electron density and EM compared to H II regions without methanol masers;
– Based on a sample of 213 H II regions within R_{Gal} spanning from 1.6 to 13.1 kpc, our best estimate of the electron temperature gradient in the Galactic disk was determined to be 372 ± 28 K kpc^{-1}. This finding is consistent with previous studies of the electron temperature gradient.

This study represents an initial step in investigating the relationship between ionized gas of H II regions and their associated natal dust clumps. In forthcoming research, our intention is to determine the physical characteristics and dynamics of the dense

molecular environments surrounding these objects. To achieve this, we have conducted observations of multiple para-H_2CO transition lines with the APEX telescope. This aims to ascertain the kinetic temperatures and spatial densities of the denser H II regions through a non-LTE model and compare the pressure of the molecular and ionized gases to assess if these H II regions are approximately in pressure equilibrium. Moreover, our future investigations will involve a comparison of the nonthermal motions of molecular and ionized gases to examine whether turbulence in the ionized phase is inherited from the molecular phase.

References

Altenhoff, W. J., Downes, D., Pauls, T., & Schraml, J. 1979, A&AS, 35, 23
Alves, M. I. R., Davies, R. D., Dickinson, C., et al. 2010, MNRAS, 405, 1654
Anderson, L. D., & Bania, T. M. 2009, ApJ, 690, 706
Anderson, L. D., Bania, T. M., Jackson, J. M., et al. 2009, ApJS, 181, 255
Anderson, L. D., Bania, T. M., Balser, D. S., & Rood, R. T. 2011, ApJS, 194, 32
Anderson, L. D., Bania, T. M., Balser, D. S., & Rood, R. T. 2012, ApJ, 754, 62
Anderson, L. D., Bania, T. M., Balser, D. S., et al. 2014, ApJS, 212, 1
Anderson, L. D., Hough, L. A., Wenger, T. V., Bania, T. M., & Balser, D. S. 2015, ApJ, 810, 42
Anderson, L. D., Wenger, T. V., Armentrout, W. P., Balser, D. S., & Bania, T. M. 2019, ApJ, 871, 145
Astropy Collaboration (Robitaille, T. P., et al.) 2013, A&A, 558, A33
Astropy Collaboration (Price-Whelan, A. M., et al.) 2018, AJ, 156, 123
Balser, D. S. 2006, AJ, 132, 2326
Balser, D. S., Rood, R. T., Bania, T. M., & Anderson, L. D. 2011, ApJ, 738, 27
Balser, D. S., Wenger, T. V., Anderson, L. D., & Bania, T. M. 2015, ApJ, 806, 199
Bania, T. M., Anderson, L. D., Balser, D. S., & Rood, R. T. 2010, ApJ, 718, L106
Bania, T. M., Anderson, L. D., & Balser, D. S. 2012, ApJ, 759, 96
Beaumont, C. N., & Williams, J. P. 2010, ApJ, 709, 791
Benjamin, R. A., Churchwell, E., Babler, B. L., et al. 2003, PASP, 115, 953
Bertin, E., & Arnouts, S. 1996, A&AS, 117, 393
Beuther, H., Bihr, S., Rugel, M., et al. 2016, A&A, 595, A32
Bihr, S., Johnston, K. G., Beuther, H., et al. 2016, A&A, 588, A97
Binder, B. A., & Povich, M. S. 2018, ApJ, 864, 136
Brand, J., & Blitz, L. 1993, A&A, 275, 67
Brand, J., Massi, F., Zavagno, A., Deharveng, L., & Lefloch, B. 2011, A&A, 527, A62
Brown, R. L., Lockman, F. J., & Knapp, G. R. 1978, ARA&A, 16, 445
Brunthaler, A., Menten, K. M., Dzib, S. A., et al. 2021, A&A, 651, A85
Carey, S. J., Noriega-Crespo, A., Mizuno, D. R., et al. 2009, PASP, 121, 76
Chen, B. Q., Li, G. X., Yuan, H. B., et al. 2020a, MNRAS, 493, 351
Chen, H.-Y., Chen, X., Wang, J.-Z., Shen, Z.-Q., & Yang, K. 2020b, ApJS, 248, 3
Churchwell, E. 2002, ARA&A, 40, 27
Churchwell, E., & Walmsley, C. M. 1975, A&A, 38, 451
Churchwell, E., Smith, L. F., Mathis, J., Mezger, P. G., & Huchtmeier, W. 1978, A&A, 70, 719
Churchwell, E., Povich, M. S., Allen, D., et al. 2006, ApJ, 649, 759
Churchwell, E., Watson, D. F., Povich, M. S., et al. 2007, ApJ, 670, 428
Clemens, D. P. 1985, ApJ, 295, 422
Contreras, Y., Schuller, F., Urquhart, J. S., et al. 2013, A&A, 549, A45
Dame, T. M., Hartmann, D., & Thaddeus, P. 2001, ApJ, 547, 792
Deharveng, L., Peña, M., Caplan, J., & Costero, R. 2000, MNRAS, 311, 329
Deharveng, L., Zavagno, A., Salas, L., et al. 2003, A&A, 399, 1135
Deharveng, L., Schuller, F., Anderson, L. D., et al. 2010, A&A, 523, A6
Dharmawardena, T. E., Bailer-Jones, C. A. L., Fouesneau, M., & Foreman-Mackey, D. 2022, A&A, 658, A166
Dokara, R., Brunthaler, A., Menten, K. M., et al. 2021, A&A, 651, A86
Dokara, R., Gong, Y., Reich, W., et al. 2023, A&A, 671, A145
Dzib, S. A., Rodríguez, L. F., Loinard, L., et al. 2013, ApJ, 763, 139
Dzib, S. A., Yang, A. Y., Urquhart, J. S., et al. 2023, A&A, 670, A9
Elmegreen, B. G., & Lada, C. J. 1977, ApJ, 214, 725
Foreman-Mackey, D. 2016, J. Open Source Softw., 1, 24
Foreman-Mackey, D., Hogg, D. W., Lang, D., & Goodman, J. 2013, PASP, 125, 306
Gao, X. Y., Reich, P., Hou, L. G., Reich, W., & Han, J. L. 2019, A&A, 623, A105
Garay, G., & Rodriguez, L. F. 1983, ApJ, 266, 263
Georgelin, Y. M., & Georgelin, Y. P. 1976, A&A, 49, 57
Gong, Y., Ortiz-León, G. N., Rugel, M. R., et al. 2023, A&A, 678, A130
Gordon, M. A., & Sorochenko, R. L. 2002, Radio Recombination Lines. Their Physics and Astronomical Applications, 282
Hales, C. A., Murphy, T., Curran, J. R., et al. 2012, MNRAS, 425, 979
Hoare, M. G., Purcell, C. R., Churchwell, E. B., et al. 2012, PASP, 124, 939
Hu, B., Menten, K. M., Wu, Y., et al. 2016, ApJ, 833, 18
Kalcheva, I. E., Hoare, M. G., Urquhart, J. S., et al. 2018, A&A, 615, A103
Keto, E., Zhang, Q., & Kurtz, S. 2008, ApJ, 672, 423
Khan, S., Pandian, J. D., Lal, D. V., et al. 2022, A&A, 664, A140
Kim, W. J., Wyrowski, F., Urquhart, J. S., Menten, K. M., & Csengeri, T. 2017, A&A, 602, A37
Kolpak, M. A., Jackson, J. M., Bania, T. M., Clemens, D. P., & Dickey, J. M. 2003, ApJ, 582, 756
Kuchar, T. A., & Clark, F. O. 1997, ApJ, 488, 224
Kurtz, S., Cesaroni, R., Churchwell, E., Hofner, P., & Walmsley, C. M. 2000, in Protostars and Planets IV, eds. V. Mannings, A. P. Boss, & S. S. Russell, 299
Lang, C. C., Goss, W. M., & Wood, O. S. 1997, ApJ, 474, 275
Lang, C. C., Goss, W. M., & Morris, M. 2001, AJ, 121, 2681
Law, C. J., Yusef-Zadeh, F., & Cotton, W. D. 2008, ApJS, 177, 515
Lockman, F. J. 1989, ApJS, 71, 469
Luisi, M., Anderson, L. D., Liu, B., et al. 2020, ApJ, 889, 96
Martins, F., Schaerer, D., & Hillier, D. J. 2005, A&A, 436, 1049
McClure-Griffiths, N. M., & Dickey, J. M. 2016, ApJ, 831, 124
McClure-Griffiths, N. M., Dickey, J. M., Gaensler, B. M., et al. 2005, ApJS, 158, 178
Medina, S. N. X., Urquhart, J. S., Dzib, S. A., et al. 2019, A&A, 627, A175
Medina, S. N. X., Dzib, S. A., Urquhart, J. S., et al. 2024, A&A, in press, https://doi.org/10.1051/0004-6361/202449885
Menten, K. M. 1991, ApJ, 380, L75
Menzel, D. H. 1968, Nature, 218, 756
Mezger, P. G., Duschl, W. J., & Zylka, R. 1996, A&A Rev., 7, 289
Nguyen Luong, Q., Motte, F., Schuller, F., et al. 2011, A&A, 529, A41
Nguyen, H., Rugel, M. R., Menten, K. M., et al. 2021, A&A, 651, A88
Nguyen, H., Rugel, M. R., Murugeshan, C., et al. 2022, A&A, 666, A59
Ortiz-León, G. N., Menten, K. M., Brunthaler, A., et al. 2021, A&A, 651, A87
Ouyang, X.-J., Chen, X., Shen, Z.-Q., et al. 2019, ApJS, 245, 12
Paladini, R., Burigana, C., Davies, R. D., et al. 2003, A&A, 397, 213
Paulson, S. T., & Pandian, J. D. 2020, MNRAS, 492, 1335
Quireza, C., Rood, R. T., Bania, T. M., Balser, D. S., & Maciel, W. J. 2006, ApJ, 653, 1226
Rathborne, J. M., Whitaker, J. S., Jackson, J. M., et al. 2016, PASA, 33, e030
Reid, M. J., Menten, K. M., Brunthaler, A., et al. 2014, ApJ, 783, 130
Reid, M. J., Dame, T. M., Menten, K. M., & Brunthaler, A. 2016, ApJ, 823, 77
Reid, M. J., Menten, K. M., Brunthaler, A., et al. 2019, ApJ, 885, 131
Reifenstein, E. C., Wilson, T. L., Burke, B. F., Mezger, P. G., & Altenhoff, W. J. 1970, A&A, 4, 357
Riener, M., Kainulainen, J., Beuther, H., et al. 2020, A&A, 633, A14
Roman-Duval, J., Jackson, J. M., Heyer, M., et al. 2009, ApJ, 699, 1153
Rubin, R. H. 1985, ApJS, 57, 349
Rygl, K. L. J., Brunthaler, A., Sanna, A., et al. 2012, A&A, 539, A79
Schmiedeke, A., Schilke, P., Möller, T., et al. 2016, A&A, 588, A143
Schneider, N., Bontemps, S., Simon, R., et al. 2006, A&A, 458, 855
Schuller, F., Menten, K. M., Contreras, Y., et al. 2009, A&A, 504, 415
Sewilo, M., Churchwell, E., Kurtz, S., Goss, W. M., & Hofner, P. 2004, ApJ, 605, 285
Shaver, P. A. 1980, A&A, 90, 34

Shaver, P. A., McGee, R. X., Newton, L. M., Danks, A. C., & Pottasch, S. R. 1983, MNRAS, 204, 53

Simpson, R. J., Povich, M. S., Kendrew, S., et al. 2012, MNRAS, 424, 244

Taylor, J. H., & Cordes, J. M. 1993, ApJ, 411, 674

Thompson, M. A., Hatchell, J., Walsh, A. J., MacDonald, G. H., & Millar, T. J. 2006, A&A, 453, 1003

Thompson, M. A., Urquhart, J. S., Moore, T. J. T., & Morgan, L. K. 2012, MNRAS, 421, 408

Tielens, A. G. G. M. 2005, The Physics and Chemistry of the Interstellar Medium (Cambridge University Press)

Urquhart, J. S., Busfield, A. L., Hoare, M. G., et al. 2007, A&A, 461, 11

Urquhart, J. S., Hoare, M. G., Purcell, C. R., et al. 2009, A&A, 501, 539

Urquhart, J. S., Hoare, M. G., Lumsden, S. L., et al. 2012, MNRAS, 420, 1656

Urquhart, J. S., Thompson, M. A., Moore, T. J. T., et al. 2013, MNRAS, 435, 400

Urquhart, J. S., Csengeri, T., Wyrowski, F., et al. 2014, A&A, 568, A41

Urquhart, J. S., Moore, T. J. T., Menten, K. M., et al. 2015, MNRAS, 446, 3461

Urquhart, J. S., König, C., Giannetti, A., et al. 2018, MNRAS, 473, 1059

Urquhart, J. S., Wells, M. R. A., Pillai, T., et al. 2022, MNRAS, 510, 3389

Walsh, A. J., Burton, M. G., Hyland, A. R., & Robinson, G. 1998, MNRAS, 301, 640

Wang, Y., Bihr, S., Rugel, M., et al. 2018, A&A, 619, A124

Wang, L., Wang, H., Liu, B., & Armentrout, W. 2023, MNRAS, 526, 423

Wenger, T. V., Balser, D. S., Anderson, L. D., & Bania, T. M. 2018, ApJ, 856, 52

Wenger, T. V., Balser, D. S., Anderson, L. D., & Bania, T. M. 2019, ApJ, 887, 114

Wenger, T. V., Dawson, J. R., Dickey, J. M., et al. 2021, ApJS, 254, 36

Wienen, M., Wyrowski, F., Schuller, F., et al. 2012, A&A, 544, A146

Wink, J. E., Wilson, T. L., & Bieging, J. H. 1983, A&A, 127, 211

Wood, D. O. S., & Churchwell, E. 1989, ApJS, 69, 831

Wright, E. L., Eisenhardt, P. R. M., Mainzer, A. K., et al. 2010, AJ, 140, 1868

Xu, Y., Li, J. J., Reid, M. J., et al. 2013, ApJ, 769, 15

Yang, A. Y., Thompson, M. A., Tian, W. W., et al. 2019, MNRAS, 482, 2681

Yang, A. Y., Urquhart, J. S., Thompson, M. A., et al. 2021, A&A, 645, A110

Yang, A. Y., Dzib, S. A., Urquhart, J. S., et al. 2023, A&A, 680, A92

Zucker, C., Speagle, J. S., Schlafly, E. F., et al. 2020, A&A, 633, A51

Appendix A: Distance determination

To investigate the physical properties of H II regions, it is crucial to know their distances. The most reliable way to calculate distances involves measuring the parallax of bright, compact objects like methanol and water masers. However, this method is very time-consuming and requires complex measurements. Additionally, because it depends on the presence of bright and compact sources, which are not always available, especially in most H II regions in our sample, it cannot be applied to all of them. The Kinematic distance, though less reliable, is easier to calculate. One can determine it using the source's radial velocity relative to the local standard of rest (V_{lsr}), obtained from molecular line observations (Urquhart et al. 2012, 2018) or RRL observations (Kolpak et al. 2003; Anderson et al. 2012), along with a model for the Galaxy's rotation curve. Numerous models for the rotation of the Milky Way Galaxy exist (Clemens 1985; Brand & Blitz 1993; Reid et al. 2014). We used the rotation curve determined by Reid et al. (2014) to estimate the kinematic distance, as it leverages all the maser parallax measurements to constrain the model. This approach has proven effective in providing kinematic distances that compare well with the maser distances. While the source velocity measurement and distance determination in the Outer Galaxy is relatively simple, the problem arises for the sources within the solar circle ($R_G < 8.34$; Reid et al. 2014). For sources within the solar circle there are two solutions for the kinematic distance for every radial velocity and line of sight. These radial distances are equally spaced on either side of the tangent point, one on the near side and other on the far side. This effect is known as the kinematic distance ambiguity (KDA). To assign a unique distance to a particular source, the KDA must be resolved.

Reid et al. (2016, 2019) developed a Bayesian maximum likelihood method that resolves the KDA by considering the relative position of the spiral arms along the line of sight and the latitude of the sources. However, this method is biased toward placing the sources in spiral arms, whereas H II regions may well be located also in interarm regions (Riener et al. 2020). Therefore, we resolved the KDA using the H I E/A method (discussed in the following subsection), and for sources where the KDA remained unresolved, we adopted the Bayesian maximum likelihood distance. Fig. A.2 shows the relationship between the kinematic distances and Bayesian maximum likelihood distances, with most sources having comparable distances by both methods.

Appendix A.1: Resolving the kinematic distance ambiguity

To determine the distances to GLOSTAR H II regions, we began by matching the sources to reliable distances reported in the literature. We used the following studies in preferential order based on reliability of reported distances : parallax distances (Reid et al. 2019), kinematic distances of the HRDS H II regions (Anderson et al. 2012), kinematic distances to known H II regions (Anderson & Bania 2009), and kinematic distances to the ATLASGAL clumps (Urquhart et al. 2018), as these studies already went through steps removing the distance ambiguity. We compared the longitude, latitude, and velocities of our sources with the positions in these studies and adopted the distance where a correlation was found. Based on this, we adopted parallax distance (Reid et al. 2019) for 28 GLOSTAR H II regions and kinematic distances (Anderson & Bania 2009; Anderson et al. 2012; Urquhart et al. 2018) for 121 GLOSTAR H II regions. For 13 GLOSTAR H II regions located toward

Cygnus X, we adopted a distance of 1.4 kpc. We did not determine distances for 29 GLOSTAR H II regions toward the Galactic center ($358° \leq \ell \leq 3°$) because kinematic distances in this region are highly unreliable. For the rest of 53 GLOSTAR H II regions we resolve the KDA.

Several methods are discussed in the literature that can be used to resolve the KDA for Galactic H II regions. In this study, we used the H I E/A method, which has proven effective for resolving the KDA for H II region (Kolpak et al. 2003; Anderson & Bania 2009; Urquhart et al. 2012; Anderson et al. 2012). H II regions emit broadband continuum free-free thermal radiation in the cm wavelength range. Neutral H I gas between the H II region and the observer will absorb this thermal emission if the brightness temperature of the H I gas is lower than that of the H II region at 21 cm. In the first quadrant, the LSR velocity increases with distance from the Sun, reaches its maximum value at the tangent point, and then decreases with further distance. Thus, H II regions at the near distance will show H I absorption up to their recombination line velocity. Conversely, H II regions at the far distance will show H I absorption from the foreground H I clouds at velocities up to the tangent point velocity. The H I E/A method relies on H I absorption between the RRL and tangent point velocity to distinguish between the near and far distances.

For H II regions which do not show absorption features above threshold, we cannot use the H I E/A method to resolve the KDA. For such sources we used H I self-absorption method (eg., Roman-Duval et al. 2009; Anderson & Bania 2009; Urquhart et al. 2018) but these distances are much less certain and reliable Anderson & Bania (2009). If even the H I self-absorption method is not conclusive we adopted the Bayesian maximum likelihood distance.

We adopted the methodology explained by Urquhart et al. (2012); Kolpak et al. (2003) for resolving the KDA of H II regions and are briefly explained below:

1. We have extracted continuum included H I spectra from the Southern Galactic Plane Survey (SGPS; McClure-Griffiths et al. 2005) and the HI/OH/Recombination line survey of the inner Milky Way (THOR; Bihr et al. 2016; Wang et al. 2018).
2. We check the 21 cm continuum association of the GLOSTAR H II regions, by extracting the 21 cm continuum emission map from the SGPS and the THOR survey and search for positional coincidence. Subsequently, we extracted the continuum-included H I spectra and spatially integrated over the GLOSTAR radio emission region to obtain a source-averaged H I spectrum toward 53 GLOSTAR H II regions.
3. As was described by Anderson & Bania (2009), the background contribution was estimated by averaging the emission within four regions as near as possible to the 21 cm source and avoiding any other nearby continuum emission. These regions around the target are selected in such a way that it compensates for any gradient that may be present in the background emission. The final spectra were produced by subtracting the background emission from the source-averaged continuum-included H I spectra. In Fig. A.1, we present a sample of the background-subtracted H I spectra obtained toward a GLOSTAR H II region.
4. Before determining the reliability of any absorption feature, we first estimated two important sources of noise in the extracted continuum-included H I spectra; these are the receiver noise (σ_{rms}) and H I emission fluctuations. We have estimated the receiver noise by calculating the standard deviation using the absorption-free channels. The second source of noise is due to H I emission fluctuation. These are present

over all angular scales and can result in positive and negative wiggles in observed spectra which creates confusion in the identification of the absorption feature. The H I emission fluctuation was estimated by calculating the standard deviation of the off-source spectra as a function of velocity. The receiver noise and H I emission fluctuation level for each spectrum were presented by gray and purple horizontal lines, respectively in Fig. A.1. We consider a reliable absorption feature if the depth of the absorption is more than four times the receiver noise and larger than the background emission fluctuation present in the spectrum.

5. Kolpak et al. (2003) assigned the near, far, or tangent-point kinematic distance designations for each source by calculating the velocity differences $V_T - V_{lsr}$ and $V_T - V_A$. They found out that there are two distinct groups of sources for which $V_T - V_{lsr} > 0$. One has $V_T - V_A$ close to 0 and is located at far distance. The other group has $V_T - V_A$ significantly greater than 0 and are located at near distance. If any source has $V_T - V_{lsr} < 0$, it must be at the tangent point. Using Kolpak et al. (2003) method, we need only three velocity measurements to resolve the KDA. We consider RRL peak velocity as source velocity. To determine the velocity of tangent point, we used the empirical relation between H I termination velocities and Galactic longitude derived by McClure-Griffiths et al. (2005); McClure-Griffiths & Dickey (2016). Finally, we measure the maximum velocity of absorption for Northern Galactic Plane, which is obtained by measuring the maximum velocity where the absorption dip is larger than four times the receiver noise (standard deviation of the absorption free channels of the H I spectrum) and larger than the value of the H I emission fluctuations. In Table C.3 we presented these velocities for each H II region. Fig. A.1 shows the plots of the background subtracted continuum-included H I spectrum toward sources where significant H I absorption is seen. On these plots the velocity of tangent point, source velocity and maximum velocity of absorption are indicated by dashed vertical red, blue, and green lines, respectively. The dashed horizontal gray and purple line shows the $4\sigma_{rms}$ threshold level determined from the receiver noise and H I emission fluctuation, respectively. The gray vertical shaded region around tangent point velocity shows the possible deviation due to streaming motions (± 10 km s^{-1}) and the vertical yellow shaded regions around the source velocity represent the FWHM of RRL.

6. To identify the positions of near, far, and tangent point sources in velocity difference space ($V_T - V_{lsr}$ vs $V_T - V_A$), Kolpak et al. (2003) conducted a simulation with 10000 randomly placed H II regions, with Galactocentric radii between 3 and 8 kpc and Galactic longitudes between 18° and 50°. This simulation allowed them to approximate the boundaries in the $V_T - V_{lsr}$ vs $V_T - V_A$ plot that correspond to high-quality KDA resolutions, as depicted in Fig. A.2. In Fig. A.2, the diagonal and horizontal shaded regions show the expected location in the velocity parameter space of the source at the near and far distance, respectively. The dark gray region represents the location of 90 percent of the simulated sources were located, and lighter shaded region shows a 10 km s^{-1} extension to the simulated data. The darker triangular region in the lower left quadrant of the plot indicates the overlapping parameter space where distance assignments are inherently more uncertain. The dashed diagonal line divides this triangle into two regions: sources above the line are more likely to be at a near
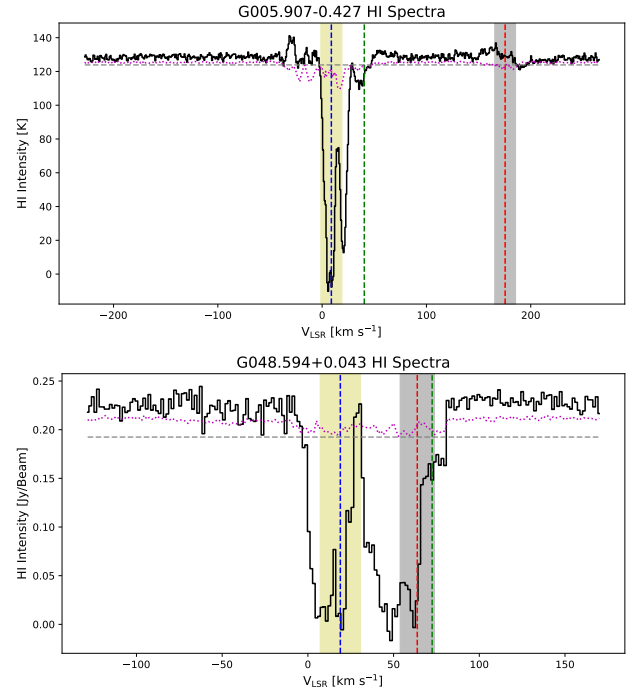
Fig. A.1. Source-averaged continuum-included H I spectra toward the H II regions extracted from the H I SGPS (top panel) and THOR survey (bottom panel). The source velocity (V_{lsr}), the velocity of tangent point (V_T), and the velocity of the first absorption minimum (V_A) are shown by the vertical dashed blue, red, and green lines, respectively. The yellow shaded region around the source velocity represents the line width of the RRL and gray shaded region around velocity of the tangent point covers 10 km s^{-1} either side and is provided to give an indication of the uncertainty associated with the streaming motion. The horizontal dashed gray and dotted purple lines show the $4\sigma_{rms}$ receiver noise level and the H I emission fluctuations, respectively. We provide example of sources placed at the near and far distance in the top and bottom panels, respectively.

distance, while those below are more likely to be at a far distance.

7. In Fig. A.2, sources which are located in the dark shaded diagonal region were assigned near distances with high degree of confidence ("n"; Quality = A), where source located in lighter shaded diagonal region assigned a near distance with low degree of confidence ("n?"; Quality = B). With this we found out of 53 GLOSTAR H II region 22 are located at near distance.

8. In Fig. A.2, sources which are located in the dark shaded horizontal region assigned a far distance with the high degree of confidence ("f"; Quality = A), where source located in lighter shaded horizontal region assigned a far distance with low degree of confidence ("f?"; Quality = B). With this we found out of 53 GLOSTAR H II region 15 are located at far distance.

9. For the sources which are located close to the tangent point velocity ($|V_{lsr} - V_T| < 10$ km s^{-1}), we assigned a tangent point distance to the source with high degree of confidence ("T"). If the source is located in the lower triangular region of Fig. A.2, we assigned a tangent point distance to the source with low degree of confidence ("T?"). With this we found out of 53 GLOSTAR H II region 11 are located at tangent point distance.

10. For the sources where the absorption dip is not larger than the threshold and we were not able to estimate the V_A, we

used H I self-absorption method to resolve the KDA. However for these sources we assigned low degree of confidence ("n?" or "f?"). For 5 sources we were not able to resolve the KDA, for these sources we adopted the Bayesian maximum likelihood distance and assigned the lower degree of confidence ("?", Quality = C).

We present the source names, radial velocities (V_{lsr}), velocity of the tangent point (V_T), velocity of the highest velocity of absorption (V_A), the Bayesian distance (Reid et al. 2019), near and far distances determined from the rotation curve (Reid et al. 2014), the kinematic solution, the assigned distance to the sources and the respective uncertainty, and quality of the solution in Table C.3.

Appendix B: Uncertainties in the derived parameters

The median uncertainty on the integrated continuum flux and ⟨Hnα⟩ amplitude estimation is ~5% and 8%, respectively, whereas the median uncertainty on the FWHM of the RRL is ~9%. The uncertainty in the electron temperature is determined by combining the uncertainties in the continuum flux, ⟨Hnα⟩ amplitude, and RRL width, in quadrature. This results in a similar level of uncertainty in the derived electron temperature; that is, $\sigma T_e/T_e = 12\%$.

The average uncertainty in estimating distances to 53 H II regions using the H I E/A method with the Reid et al. (2014) Galactic rotation curve is 17%. This aligns with the findings of Wenger et al. (2018), who reported a median uncertainty of 28% for kinematic distance estimates using the same rotation curve. The median uncertainty in parallax distances (Reid et al. 2019) is 10%, while the uncertainty for distances to HRDS H II regions (Anderson et al. 2012) is 5%. In Urquhart et al. (2018) and Anderson & Bania (2009), the typical distance uncertainty is about 10%. Overall, the median distance uncertainty for GLOSTAR H II regions is ~10%. The resultant errors in the EM, electron density, Lyman continuum photon rate and ionized gas mass estimations obtained using SOERP python package are 8%, 6%, 21%, and 26%, respectively. For some sources, the uncertainty in the derived physical properties exceeds 50% (e.g., G010.197-0.424), primarily due to very high uncertainty in the distance estimation.

Appendix C: Tables
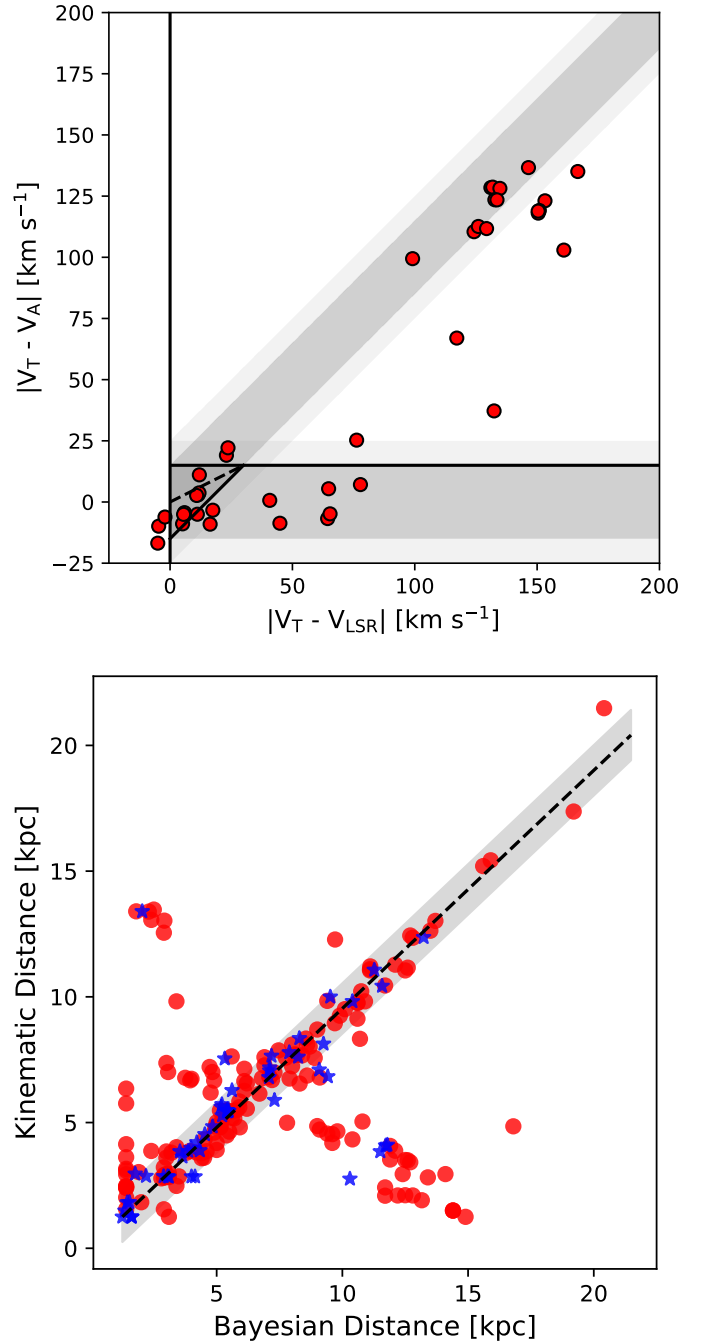
Fig. A.2. Top panel: Plot showing the difference in source velocity (V_{lsr}) and the velocity of tangent point (V_T), versus the difference in the velocity of the first absorption minimum (V_A) and the V_T. The diagonal and horizontal shaded regions represent the expected location of the near and far distance sources, respectively, while the solid line shows the approximate boundaries (Kolpak et al. 2003; Urquhart et al. 2012). The dashed diagonal line divides the darker triangular region in the lower left quadrant of the plot into two regions: sources above the line are more likely to be at a near distance, while those below are more likely to be at a far distance. Bottom panel: Plot showing the relation between the distance determined using the Bayesian method presented by Reid et al. (2016, 2019) and the near/far distance determined using the Reid et al. (2014) rotation curve. The red circles and blue stars represent the distances taken from literature and obtained distance for 53 H II regions, respectively. The solid black line shows the line of equality, and the gray shaded region represents ±1 kpc.

Table C.1. GLOSTAR H II region catalog with continuum and stacked ⟨Hnα⟩ hydrogen RRL parameters.

Name [a]	GLOSTAR Name [b]	l_{peak} [°]	b_{peak} [°]	S_{peak} [Jy Beam^{-1}]	S_C [mJy]	σS_C [mJy]	S_L [mJy]	σS_L [mJy]	ΔV [kms^{-1}]	$\sigma \Delta V$ [kms^{-1}]	V_{LSR} [kms^{-1}]	σV_{LSR} [kms^{-1}]	D_{sun} [c] [kpc]	σD_{sun} [kpc]	R_{Gal} [kpc]	Morphology [d]	ATLASGAL Clump [e]	CH$_3$OH [f]
⋮	⋮	⋮	⋮	⋮	⋮	⋮	⋮	⋮	⋮	⋮	⋮	⋮	⋮	⋮	⋮	⋮	⋮	⋮
G031.474-0.344	G031.476-00.344	31.474	-0.344	0.07	261.75	14.24	26.27	3.94	28.84	5.0	89.62	2.12	9.0	0.7	4.72	IB		⋮
G032.059+0.080	G032.063+00.078	32.059	0.08	0.03	157.28	11.34	21.23	3.23	23.9	4.19	98.86	1.78	7.2	0.0	4.34	B		⋮
G032.150+0.133	G032.15+00.133	32.15	0.133	0.51	681.96	34.22	46.24	1.99	26.49	1.32	97.46	0.56	6.2	0.62	4.39	IB	AGAL032.149+00.134	⋮
G032.272-0.225	G032.272-00.226	32.272	-0.225	0.29	320.89	16.15	12.57	1.31	23.59	2.85	21.34	1.21	12.8	0.5	7.34	C	AGAL032.272-00.226	⋮
G032.589+0.008	G032.590+00.010	32.589	0.008	0.02	173.41	9.78	20.59	3.87	15.95	3.46	80.37	1.47	9.4	0.6	5.07	PB		
G032.797+0.191	G032.798+00.191	32.797	0.191	2.71	3129.42	156.55	121.92	2.15	33.04	0.67	16.18	0.29	9.71	2.92	5.26	C	AGAL032.797+00.191	G032.8027+0.1926
G032.927+0.606	G032.928+00.606	32.927	0.606	0.29	328.51	16.51	12.7	2.24	27.42	5.58	-34.95	2.37	19.2	1.5	13.13	C	AGAL032.926+00.606	
G032.990+0.040	G032.991+00.039	32.99	0.04	0.14	188.07	10.79	17.69	2.05	22.82	3.06	91.56	1.3	8.6	0.86	4.78	B		G032.9918+0.0343
G033.204-0.009	IRAS 18494+0010	33.204	-0.009	0.09	374.08	21.28	31.7	3.51	22.51	2.87	107.49	1.22	7.1	0.71	4.47	IB	AGAL033.206-00.009	G033.2037-0.0101
G033.419-0.004	G033.418-00.004	33.419	-0.004	0.13	196.04	10.33	10.93	1.4	34.3	5.07	63.49	2.15	9.4	0.94	5.19	C		⋮
G033.810-0.189	G033.81-00.188	33.81	-0.189	0.22	309.83	15.68	18.57	2.59	21.13	3.4	39.6	1.45	11.7	1.17	6.7	PB	AGAL033.811-00.187	⋮
G033.915+0.110	G033.914+00.110	33.915	0.11	0.82	991.23	49.67	52.58	1.86	34.62	1.42	100.02	0.6	7.1	0.71	4.56	IB	AGAL033.914+00.109	⋮
G034.089+0.436	G034.089+00.436	34.089	0.436	0.11	241.65	12.99	19.24	3.04	16.95	3.09	34.26	1.31	12.2	1.22	7.11	IB	AGAL034.089+00.436	⋮
G034.132+0.471	G034.133+00.471	34.132	0.471	0.41	518.68	26.22	30.94	3.03	21.16	2.39	34.4	1.02	11.7	0.5	6.74	B	AGAL034.133+00.471	⋮
G034.255+0.146	CORNISH G034.2544+00.1460	34.255	0.146	2.25	8087.97	405.24	532.43	6.7	25.25	0.37	54.04	0.16	3.4	0.34	5.67	IB		⋮
G034.257+0.153 [*]	CORNISH G034.2573+00.1523	34.257	0.153	2.29	2440.25	122.65	39.35	1.48	59.79	2.6	44.09	1.1	3.4	0.34	5.67	C	AGAL034.258+00.154	G34.2582+0.1534
G034.322+0.160	G034.322+0.160	34.322	0.16	0.03	102.1	17.61	13.67	1.22	31.49	3.23	53.8	1.37	10.4	0.35	5.88	ND		⋮
⋮	⋮	⋮	⋮	⋮	⋮	⋮	⋮	⋮	⋮	⋮	⋮	⋮	⋮	⋮	⋮	⋮	⋮	⋮

Notes. The entire table is accessible in a machine-readable format at the CDS. A section of the table is provided here as a reference for its format and content. [a] G*lll.lll*+*b.bbb* where l and b is the position of peak pixel. [b] Name of the corresponding GLOSTAR continuum source located within angular separations of 36″ in the GLOSTAR VLA D-configuration continuum source catalog (Medina et al. 2019, 2024). For sources where no crossmatch was found due to contamination from extended large-scale structures, we provided the name of the nearest H II region in the SIMBAD database. [c] References for distances: (1) Reid et al. (2019); (2) Anderson et al. (2012); (3) Anderson & Bania (2009); (4) Urquhart et al. (2018). [d] Classification of source based on *Spitzer* GLIMPSE 8 µm emissions, as is explained in Section 5.1. [e] Name of the associated ATLASGAL dust clump (Urquhart et al. 2014) (see Section. 5.2). [f] Name of the associated 6.7 GHz methanol (CH$_3$OH) maser (Nguyen et al. 2022) (see Section. 4.3.2). [*] Candidate HC H II regions (see Section. 5.3).

Table C.2. Physical properties of the GLOSTAR H II regions.

Name	θ_{source} ['']	d_{eff} [pc]	T_e [10^3 K]	σT_e [10^3 K]	EM [10^5 pc cm^{-6}]	σEM [10^5 pc cm^{-6}]	n_e [10^2 cm^{-3}]	σn_e [10^2 cm^{-3}]	N_{Lyc} [10^{48} s^{-1}]	σN_{Lyc} [10^{48} s^{-1}]	Mass$_{H II}$ [$M_\odot$]	σMass$_{H II}$ [$M_\odot$]
.	.	.	.	.	.	.	.	.	.	.	.	.
.	.	.	.	.	.	.	.	.	.	.	.	.
G031.474-0.344	81.24	3.54	4.1	0.9	0.28	0.03	0.89	0.06	2.82	0.52	50.99	11.89
G032.059+0.080	99.73	3.48	3.8	0.8	0.11	0.01	0.55	0.03	1.13	0.11	32.64	4.15
G032.150+0.133	56.24	1.69	6.3	0.5	1.75	0.12	3.21	0.2	2.89	0.59	14.4	3.66
G032.272-0.225	50.66	3.14	11.1	1.7	1.24	0.1	1.99	0.09	4.47	0.47	36.04	4.74
G032.589+0.008	100.87	4.6	6.0	1.6	0.14	0.02	0.54	0.04	1.73	0.3	50.82	11.47
G032.797+0.191	49.75	2.34	8.4	0.4	11.33	0.75	6.96	1.12	28.58	17.61	65.74	51.9
G032.927+0.606	52.44	4.88	9.9	2.5	1.14	0.12	1.53	0.1	10.87	2.09	114.04	28.16
G032.990+0.040	55.42	2.31	5.4	0.9	0.47	0.04	1.43	0.1	1.65	0.36	18.47	5.0
G033.204-0.009	100.87	3.47	5.9	0.9	0.29	0.03	0.92	0.06	2.13	0.46	37.16	9.99
G033.419-0.004	50.21	2.29	5.9	1.1	0.62	0.06	1.64	0.11	1.96	0.43	19.08	5.24
G033.810-0.189	56.64	3.21	8.5	1.7	0.87	0.08	1.65	0.11	4.08	0.9	39.7	11.06
G033.915+0.110	52.44	1.81	6.1	0.4	2.9	0.2	4.01	0.24	5.56	1.14	22.21	5.63
G034.089+0.436	75.09	4.44	8.0	1.8	0.38	0.04	0.92	0.07	3.55	0.8	61.5	17.58
G034.132+0.471	54.58	3.1	8.5	1.2	1.57	0.13	2.25	0.1	6.83	0.74	48.5	6.55
G034.255+0.146	99.04	1.63	6.7	0.3	6.84	0.45	6.47	0.39	10.01	2.03	24.75	6.23
G034.257+0.153 (∗)	46.91	0.77	10.7	0.7	10.86	0.74	11.85	0.72	2.44	0.5	3.3	0.84
G034.322+0.160	72.29	3.64	3.0	0.6	0.12	0.03	0.58	0.07	1.7	0.23	47.07	5.32
.	.	.	.	.	.	.	.	.	.	.	.	.
.	.	.	.	.	.	.	.	.	.	.	.	.

Notes. The entire table is accessible in a machine-readable format at the CDS. A section of the table is provided here as a reference for its format and content.
$^{(∗)}$Candidate HC H II regions (see Section. 4.3.2)

Table C.3. Kinematic distance analysis of 53 GLOSTAR H II regions.

Name	ℓ_{peak}	b_{peak}	V_{LSR}	V_T	V_A	Reid Distance			n/f/?	D_{sun}	σD_{sun}	Quality
						Bayesian	Near	Far				
	[°]	[°]	[km s^{-1}]	[km s^{-1}]	[km s^{-1}]	[kpc]	[kpc]	[kpc]		[kpc]	[kpc]	
G005.907-0.427	5.907	-0.427	8.83	175.45	40.4	2.96	1.76	13.8	n?	1.76	0.74	B
G008.662-0.342	8.662	-0.342	36.12	167.22	38.75	2.85	4.14	12.02	n	4.14	0.45	A
G008.872-0.319	8.872	-0.319	34.77	166.6	37.93	2.85	4.0	12.14	n	4.0	0.48	A
G010.597-0.384	10.597	-0.384	0.56	161.48	58.54	4.84	0.73	15.66	?	4.84	0.48	C
G010.197-0.424	10.197	-0.424	9.45	162.66	39.58	1.25	1.25	14.42	n?	1.25	1.04	B
G010.142-0.422	10.142	-0.422	11.92	162.82	43.7	1.25	1.61	14.13	n?	1.61	0.96	B
G010.069-0.425	10.069	-0.425	16.58	163.04	26.39	2.87	2.19	13.66	n	2.19	0.8	A
G010.229-0.297	10.229	-0.297	12.11	162.57	44.52	1.25	1.62	14.12	n?	1.62	0.94	B
G010.229-0.349	10.229	-0.349	12.14	162.57	43.7	1.25	1.62	14.12	n?	1.62	0.94	B
G012.805-0.224	12.805	-0.224	30.75	154.97	44.52	2.86	3.05	12.86	n	3.05	0.5	A
G012.192-0.104	12.192	-0.104	24.36	156.77	119.55	12.37	2.64	13.23	f?	13.23	0.51	B
G012.724-0.225	12.724	-0.225	38.04	155.21	88.22	3.85	3.54	12.43	n	3.54	0.51	A
G012.912-0.282	12.912	-0.282	28.67	154.65	42.05	2.86	2.89	13.0	n	2.89	0.52	A
G013.184+0.050	13.184	0.05	54.75	153.86	54.42	3.89	4.33	11.69	n	4.33	0.31	A
G014.597+0.020	14.597	0.02	20.39	149.73	38	13.4	2.04	13.66	n	2.04	0.61	A
G014.619+0.118	14.619	0.118	34.85	149.66		2.84	3.1	12.72	n?	3.1	0.44	B
G015.137-0.529	15.137	-0.529	13.37	148.16	20	1.49	1.35	14.24	n	1.35	0.7	A
G015.189-0.599	15.189	-0.599	15.27	148	24.5	1.83	1.53	14.08	n	1.53	0.67	A
G015.205-0.627	15.205	-0.627	14.36	147.96	24.5	1.82	1.44	14.16	n	1.44	0.69	A
G019.117-0.337	19.117	-0.337	65.99	136.71		4.21	4.21	11.37	n	4.21	0.28	A
G020.740-0.085	20.74	-0.085	54.31	132.11	125	4.11	3.6	11.79	f	11.79	0.3	A
G020.682-0.157	20.682	-0.157	56.04	132.28	107	4.08	3.68	11.72	f?	11.72	0.3	B
G023.437-0.209	23.437	-0.209	101.56	124.59	105.5	7.54	5.32	9.86	n	5.32	0.26	A
G023.384-0.142	23.384	-0.142	98.61	124.74		5.28	5.22	9.97	n	5.22	0.26	A
G024.507-0.222	24.507	-0.222	97.98	121.65	99.5	5.62	5.18	9.87	n	5.18	0.27	A
G024.402+0.071	24.402	0.071	110.49	121.93	119	6.83	5.66	9.42	f?	9.42	0.27	B
G024.712-0.125	24.712	-0.125	109.12	121.09	110	6.28	5.61	9.43	n?	5.61	0.28	B
G025.692+0.031	25.692	0.031	53.63	118.42	113	3.85	3.32	11.51	f	11.51	0.31	A
G025.479-0.174	25.479	-0.174	55.8	118.99		3.87	3.43	11.43	?	3.87	0.44	C
G025.275-0.317	25.275	-0.317	67.45	119.55		3.64	3.95	10.96	?	3.64	0.35	C
G027.994-0.022	27.994	-0.022	100.64	112.23		5.89	5.34	9.27	T?	7.3	0.32	B
G028.569+0.020	28.569	0.02	98.88	110.71	107	8.13	5.28	9.25	f?	9.25	0.32	B
G028.977-0.607	28.977	-0.607	51.67	109.63		3.98	3.13	11.26	?	3.98	0.8	C
G029.859-0.059	29.859	-0.059	97.99	107.32		7.65	5.3	9.05	T	7.18	0.36	A
G030.252+0.053	30.252	0.053	70.29	106.29		4.53	4	10.26	?	4.53	0.83	C
G030.687-0.072	30.687	-0.072	94.32	105.17	102.5	7.06	5.15	9.07	T?	7.11	0.36	B
G030.750+0.013	30.75	0.013	93.85	105	110	7.1	5.13	9.08	f	9.08	0.36	A
G030.789-0.100	30.789	-0.1	108.74	104.9		7.18	6.05	8.17	T	7.11	0.47	A
G030.854+0.151	30.854	0.151	40.34	104.73	111.5	10.43	2.52	11.58	f	11.58	0.36	A
G031.147+0.275	31.147	0.275	108.97	103.98		6.8	6.13	8.03	T	7.08	0.5	A
G034.322+0.160	34.322	0.16	53.8	95.94		9.82	3.19	10.4	f	10.4	0.35	A
G035.035-0.504	35.035	-0.504	53.44	94.17	93.5	2.76	3.18	10.3	f	10.3	0.36	A
G043.182-0.027	43.182	-0.027	9.78	75.16	80	11.07	0.63	11.27	f	11.27	0.44	A
G043.185-0.525	43.185	-0.525	57.69	75.15	78.5	7.61	3.77	8.24	f	8.24	0.53	A
G045.132+0.143	45.132	0.143	54.57	70.94	80	7.79	3.71	7.89	f	7.89	0.53	A
G048.594+0.043	48.594	0.043	18.93	63.82	72.5	10	1.3	9.52	f	9.52	0.47	A
G048.914-0.285	48.914	-0.285	68.21	63.18	80	5.46	5.48	5.48	T	5.48	0.82	A
G049.205-0.342	49.205	-0.342	67.27	62.61	72.5	5.44	5.45	5.45	T	5.45	0.82	A
G049.477-0.329	49.477	-0.329	56.96	62.07	71	5.48	5.42	5.42	T	5.42	0.82	A
G049.585-0.385	49.585	-0.385	63.94	61.86	68	5.43	5.41	5.41	T	5.41	0.82	A
G049.440-0.459	49.44	-0.459	56.26	62.15	66.5	5.48	5.42	5.42	T	5.42	0.82	A
G051.365-0.012	51.365	-0.012	52.93	58.45	63.5	5.72	5.21	5.21	T	5.21	0.84	A
G059.800+0.231	59.8	0.231	-2.07	44.11		8.35	0.1	8.29	f?	8.29	0.55	B